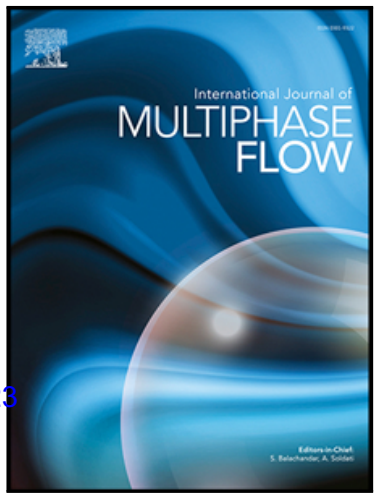
Accepted Manuscript



Development of a new multiphase sediment transport model for free surface flows

Mohamed Ouda , Erik A. Toorman

PII: S0301-9322(18)30846-2
DOI: https://doi.org/10.1016/j.ijmultiphaseflow.2019.04.023
Reference: IJMF 3028

To appear in: *International Journal of Multiphase Flow*

Received date: 21 November 2018
Revised date: 13 March 2019
Accepted date: 24 April 2019

Please cite this article as: Mohamed Ouda , Erik A. Toorman , Development of a new multiphase sediment transport model for free surface flows, *International Journal of Multiphase Flow* (2019), doi: https://doi.org/10.1016/j.ijmultiphaseflow.2019.04.023

This is a PDF file of an unedited manuscript that has been accepted for publication. As a service to our customers we are providing this early version of the manuscript. The manuscript will undergo copyediting, typesetting, and review of the resulting proof before it is published in its final form. Please note that during the production process errors may be discovered which could affect the content, and all legal disclaimers that apply to the journal pertain.

ACCEPTED MANUSCRIPT

Highlights

- New multiphase model for sediment transport in free surface flows was developed.
- μ(I) rheology was successfully employed to model the particle-particle interaction.
- The newly developed model was validated and successfully used to model sediment transport in free surface flow including waves' condition.
- k-ε turbulence model requires significant improvements in order to be suitable for multiphase flow simulations.

ACCEPTED MANUSCRIPT

ACCEPTED MANUSCRIPT

Development of a new multiphase sediment transport model for free surface flows

Mohamed Ouda[1, a, b] **& Erik A. Toorman** [a]

a. Hydraulics Laboratory, Department of Civil Engineering, KU Leuven Kasteelpark Arenberg 40, box 2448, B-3001 Leuven, Belgium
b. Transportation Engineering Department, Alexandria University, Alexandria 21544, Egypt

E-mail: mohamed.ouda@kuleuven.be, erik.toorman@kuleuven.be

Abstract

Modeling of sediment transport in estuaries and coastal areas requires a lot of compromises to keep the computational costs within acceptable limits. Due to that, existing sediment transport models do not account for particle-scale physics, e.g. particle-particle interaction and turbulence modulation by sediment, which play a significant role, especially in the non-dilute regime. In the current study, a newly developed physics-based sediment transport model for free surface flows and its numerical implementation within the OpenFOAM framework is introduced. The new model is based on the multiphase mixture theory to account for interactions between sediment and water while tracking the free surface at the same time. A modified VOF equation for sediment-laden free surface flow was derived and implemented. The interphase momentum transfer is considered by solving an additional closure for the slip velocity which includes the effects of drag force, turbulent dispersion, and shear-induced diffusion. Dense granular flow rheology is used to supply the required closures for particle stresses. Additionally, suitable closures for the mixture and turbulent viscosities are introduced. The model was validated using experimental data and analytical solutions of five test cases of variable complexity. This includes pure sedimentation, laminar bedload transport, turbulent sheet flow, local scour due to a submerged jet, and wave-induced scour under a submarine pipeline.

Keywords

Multiphase flow theory; mixture theory; high-concentrated sediment transport; slip velocity; dense granular flow rheology, OpenFOAM.

ACCEPTED MANUSCRIPT

[1] Corresponding author

ACCEPTED MANUSCRIPT

1. Introduction

Sediment transport in free surface flows is, intrinsically, a multiphase problem since it involves motion and interactions between three distinct phases, namely: sediment, water, and air. It is a ubiquitous phenomenon in nature, e.g. sediment transport in rivers, estuaries and coastal areas, qualitatively rather well understood, yet poorly quantifiable.

This phenomenon has been subjected to extensive research during the past decades. However, there are few studies that address sediment transport at scales of practical engineering interest from the multiphase perspective. This is usually attributed either to the lack of understanding of the underlying physics or due to the fact that the multiscale physics are so complicated and expensive to be included in a numerical model that can be applied to any practical scale.

Sediment transport physics includes not only the fundamental macro-scale processes of entrainment, transport, and deposition but also the sub-grid scale processes that derive the macro-scale ones. According to Toorman et al. [118], the most important sub-grid scale processes are interphase momentum transfer, sub-grid scale roughness, particle-fluid-turbulence interaction, and near-bed layer process. In addition to micro and macro-scale processes, the presence of the free surface enriches the flow dynamics and increases the complexity of its modelling.

In most sediment transport models that are widely used for large-scale applications, some of those processes are parametrized in a purely empirical way (e.g. the effect of bedforms on the roughness length), while others are poorly described or even totally neglected (e.g. particle turbulence interaction and interphase momentum transfer, which are often unconsciously accounted for by tuning the bottom friction parameter without under-standing or even realizing the physics behind the necessity to vary this parameter).

Comprehensive reviews of the existing traditional models for non-cohesive sediment transport in coastal areas are provided by Papanicolaou et al. [103], Amoudry [1], Wong [129], Copper [38], and Roelvink [108] among others. From those reviews, we can see that there is an ample variety of sediment transport models that have different features and can operate in 1D, 2D or 3D. However, all those model share the same fundamental concept and structure.

In those models, the water-sediment mixture is modeled as a single phase fluid for which the 3D Reynolds Averaged Navier-Stokes equations or 3D or 2D Shallow water equations are solved first to obtain the hydrodynamic parameters (velocity, pressure, water depth etc.). The sediment phase is treated as a passive scalar, i.e. the sediment particles are strictly following the fluid motion except in the vertical direction where the particles are moving with the sum of flow and settling velocity.

The flow domain is divided into two regimes based on the sediment concentration: dilute or suspended load regime and non-dilute or bedload regime. For the dilute sediment suspension, an advection-diffusion equation forced by the known flow velocity is used to predict the sediment concentration evolution. While for the near-bed highly concentrated layer, because its thickness is of subgrid scale, an empirical bedload formula is used to calculate the bedload sediment flux.

Due to this treatment of the sediment phase, many flaws have emerged in the traditional models. For instance, the nearly passive scalar hypothesis implies no-slip velocity or momentum transfer between the different phases. This means that the particle's feed-

ACCEPTED MANUSCRIPT

back effect on the fluid flow and turbulence (two-way coupling) is neglected (except for buoyancy effects).

This momentum transfer between particle and fluid are noticeable and can modulate turbulence structure of the fluid phase when the sediment volume fraction exceeds 10^{-5} [49].

Moreover, the assumption that the fluid and particle are moving at the same velocity has been discredited based on many experimental observations. The experimental data show that the particle velocity lags behind the fluid velocity for non-buoyant particles [13, 34, 99], and the velocity profile in sediment-laden flow deviates from that in the clear water [6, 21, 48, 58, 104].

For the concentration profile, the theoretical solution of the sediment advection-diffusion equation is simply equivalent to the Rouse profile [109]. This profile is found to be significantly different when compared to the experimental observations [56, 65, 133]. An important reason for this is the difficulty of making an accurate estimate of the near-bottom concentration, which has to be imposed as a boundary condition to solve the mass balance equation.

Accordingly, the suspended sediment flux, which is calculated by integrating the product of particle velocity and sediment concentration profiles, is expected to deviate from the measurements. One of the discrepancies is related to the implicit assumption by Rouse that the turbulent diffusion coefficient of mass (the eddy diffusivity) is equal to that of momentum (the eddy viscosity). This has subsequently been corrected by introduction of an empirical correction factor, the turbulent Schmidt number, which later, based on two-phase flow theory, has been shown to be more complicated [119, 120].

Traditional sediment transport models also do not resolve the near-bed highly concentrated layer because the vertical scale used in those models is much larger than the thickness of this layer which only extends to few centimeters above the bed [3]. In this layer, the sediment volume fraction is well beyond the 10^{-3} limit at which the particle-particle interaction (four-way coupling) becomes a significant momentum transfer mechanism [49].

It is this mechanism that is responsible for giving the highly concentrated mixture its interesting rheological characteristics. Mutual collisions and enduring contacts give rise to the particle pressure and particle shear stress. In the highly concentrated region, this leads to a sharp increase in the effective mixture viscosity and at the packing limit the mixture behaves as a solid.

Due to those discrepancies, the need for a more physics-based sediment transport model that incorporates the micro-scale processes became demanding. In the past decade, many models have been developed based on multiphase flow theory to fulfill this requirement. Those models fall into two main categories: Eulerian-Eulerian or Eulerian-Lagrangian.

In the Eulerian-Eulerian framework, all phases are treated as continua but with different constitutive equations for pressure, shear stress and viscosity. Momentum and continuity equations are solved for each phase. To model the coupling between the different phases, an interphase momentum transfer term, as a function of drag, lift, buoyancy and added forces, is added to the momentum equation. Many models have been introduced based on this framework, e.g. Drew [44], Kobayashi [82] ,Cao [22], Greimann [56], Hsu

ACCEPTED MANUSCRIPT

et al. [64], Chauchat [26, 29, 30], Amoudry [2], Toorman[119], Jha [74], Lalli et al. [84], Cheng [35], and Lee et al. [89].

In the Eulerian-Lagrangian framework, the fluid phase is modeled as continuum while the sediment phase is modeled as discrete particles, whose position and velocity is tracked by solving the force balance equation (momentum equation in Lagrangian form) for each particle. Models based on this framework have been introduced by e.g. Drake and Calantoni [43], Schmeeckle [112], Sun and Xiao [116], and Finn et al [52]. This approach is more computationally demanding and the required computational power scales with the number of particles. Therefore, it is not practical to use this approach to model the transport of fine to medium sediment [36].

Out of many multiphase sediment transport models, there are few models that include air as third phase and handle the free surface tracking e.g. Bohorquez [15] , Kim et al. [81], and Lee et al. [90]. Tracking the free surface is essential for flows near hydraulic, coastal or offshore structures as well as the flows that incorporate surface wave motion.

In the current study, we introduce a new sediment transport flow model based on multiphase flow theory considering a system consisting of three phases: dispersed (i.e. sand), liquid (i.e. water) and gaseous (i.e. air). Mixture theory is used to derive the mixture momentum and continuity equations which are solved together with the sediment mass conservation equation. The liquid phase conservation equation is formulated and solved based on the volume of fluid (VOF) method [60]to track the water-air interface.

The interphase momentum transfer is considered by solving an additional closure for the slip velocity which includes the effects of drag force, turbulent dispersion force, and shear-induced diffusion. Dense granular flow rheology is used to supply the required closures for particle stresses. Additionally, the suitable closure for the mixture and turbulent viscosities are introduced. The system of equations is discretized following the finite volume method procedure using the numerical schemes available in the open source CFD library OpenFOAM [126].

2. Mathematical Model

The starting point for developing any multiphase model is usually the local instant formulation (LIF) which consists of field equations applied within the distinct phases complemented with jump condition to match the solution at the interface between phases [67]. This set of equations cannot be used directly due to many difficulties, especially the discontinuity at the interface and the fluctuations in all variables due to turbulence and interface motion.

So, almost in all cases, a suitable averaging technique must be applied to LIF which leads to an averaged equations in terms of mean value of the flow variables while the fluctuating part is described in a statistical way for which an appropriate closure should be supplied. Many averaging techniques can be used, e.g., time averaging [67], volume averaging [68] or ensemble averaging [45]. In the current study, we are using the averaged balance equations of a multi-fluid model derived by Ishii and Hibiki [67] as a starting point. Those equations were derived by applying the time averaging on the mass-weighted values of the variables. This is also called Favre averaging [51].

The mass and momentum conservation equations for the *k*-phase in a multiphase flow system are given by:

$$\frac{\partial \alpha_k \rho_k}{\partial t} + \nabla \bullet \left(\alpha_k \rho_k \mathbf{v}_k \right) = 0 \tag{1}$$

$$\frac{\partial \alpha_k \rho_k \mathbf{v}_k}{\partial t} + \nabla \bullet \left(\alpha_k \rho_k \mathbf{v}_k \mathbf{v}_k \right) = -\nabla \bullet \alpha_k p_k \boldsymbol{I} + \nabla \bullet \left[\alpha_k \left(\bar{\bar{\tau}}_k + \tau_k^T \right) \right] + \alpha_k \rho_k \boldsymbol{g} + \boldsymbol{M}_k , \tag{2}$$

where k stands for different phases, either water (w), sediment (s), or air (a) in the current study. α_k , ρ_k are the phase volume fraction and density, respectively. The velocity ($\boldsymbol{v}_k$) is the mass-weighted phase velocity. $\bar{\bar{\tau}}_k$, τ_k^T represent the viscous and turbulent shear stress, respectively. $\boldsymbol{M}_k$ is the interphase momentum transfer term. In Eq. (1) and (2) we consider that no phase change (e.g. no evaporation) takes places between different phases.

To obtain the mixture balance equations for the three-phase system, we need to introduce some basic mixture definitions. The mixture density (ρ) is readily given by:

$$\rho = \sum_k \alpha_k \rho_k = \alpha_s \rho_s + \alpha_w \rho_w + \alpha_a \rho_a \tag{3}$$

The mixture mass weighted velocity or velocity of center of mass is defined following [67] as:

$$\mathbf{v} = \frac{1}{\rho} \sum_k \alpha_k \rho_k \mathbf{v}_k = \frac{\alpha_s \rho_s \mathbf{v}_s + \alpha_w \rho_w \mathbf{v}_w + \alpha_a \rho_a \mathbf{v}_a}{\rho} \tag{4}$$

And the mixture volumetric flux or the mixture center of volume velocity is defined as:

$$\boldsymbol{j} = \sum_k \alpha_k \mathbf{v}_k = \alpha_s \mathbf{v}_s + \alpha_w \mathbf{v}_w + \alpha_a \mathbf{v}_a \tag{5}$$

Finally, the relative velocity between the dispersed and continuous phase is given by:

$$\mathbf{w} = \mathbf{v}_s - \mathbf{v}_c , \tag{6}$$

where $\mathbf{v}_c$ is the velocity of the continuous phase, which can be water or air.

The mixture mass conservation equation is obtained by taking the sum of Eq. (1) over all phases. Using the definitions in Eq. (3) and (4), it can be written as:

$$\frac{\partial \rho}{\partial t} + \nabla \bullet (\rho \mathbf{v}) = 0 \tag{7}$$

A more OpenFOAM-friendly version of Eq. (7) can be obtained by dropping ρ_k from Eq. (1) (since it is constant) before summation. This will yield:

$$\nabla \bullet (\boldsymbol{j}) = 0 \tag{8}$$

Equation (8) will be used to derive the mixture pressure Poisson equation. It also shows that the mixture center of volume velocity field is divergence-free while its center of mass velocity is not. This is a very important conclusion since many existing models usually use $\mathbf{v}$ instead of $\boldsymbol{j}$ in Eq. (8) to derive the mixture pressure equation. This, as will follow, causes ignoring some important terms in the final pressure equation.

The volume conservation equation for the sediment phase is simply Eq. (1) with replacing the *k*-phase by sediment and dropping the density from all terms:

ACCEPTED MANUSCRIPT

ACCEPTED MANUSCRIPT

$$\frac{\partial \alpha_s}{\partial t} + \nabla \bullet \left(\alpha_s \mathbf{v}_s \right) = 0 \tag{9}$$

In the framework of a mixture model, the velocities of distinct phases are not solved for explicitly. Alternatively, the mixture velocity and relative velocities are prognostic variables. So, Eq. (9) cannot be used directly in this form. Instead, the sediment velocity can be described as a function of the mixture and relative velocities. So, Eq. (9) can be written as (detailed derivation can be found in Appendix A):

$$\frac{\partial \alpha_s}{\partial t} + \nabla \bullet \left(\alpha_s \mathbf{v} \right) + \nabla \bullet \left[\alpha_s \left(\frac{\alpha_w}{\gamma} - \frac{\alpha_w \alpha_s \left(\rho_s - \rho_w \right)}{\rho} + \frac{\alpha_s \alpha_w \alpha_a \left(1 - S \right)}{\gamma \left(\alpha_w + \alpha_s S \right)} \right) \mathbf{w} \right] = 0, \tag{10}$$

where $S = \rho_s / \rho_w$ is the specific gravity of sand and $\gamma = \alpha_w + \alpha_s$. The 2nd term in the LHS of Eq. (10) represents the sediment volumetric flux due to the averaged mixture velocity while the 3rd term represents the relative sediment fluxes due to the slip between sediment and water or air.

To track the free surface, an additional equation needs to be solved. In the present study, the volume of fluid (VOF) method [60] is used to achieve this objective. The current implementation of the VOF method in OpenFOAM is based on the two-phase formulation where the two phases are water and air. In this implementation, the water-air mixture is considered as a single phase with variable density and viscosity. The volume conservation equation is solved in this method to track the phase indicator function or simply the water volume fraction α_w which is equal to 1.0 in water, 0 in air, and ranges from 0 to 1.0 at the air-water interface [110].

In order to derive a conservation equation for free surface tracking that is valid in the presence of sediment, starting from Eq. (1), the following relation is obtained after dropping the density:

$$\frac{\partial \alpha_w}{\partial t} + \nabla \bullet \left(\alpha_w \mathbf{v}_w \right) = 0 \tag{11}$$

Following the same reasoning, the water velocity has to be replaced by the mixture and relative velocities. Here, the additional "artificial" relative velocity, namely the relative velocity between water and air at their mutual interface, has to be considered. From a physical point of view, the boundary condition at the free surface is a no-slip condition in both tangential and normal directions [40, 67]. However, to avoid smearing of the interface, OpenFOAM adds an artificial compression velocity ($\mathbf{U}_c$) which acts normal to the interface [125]. This velocity is given by:

$$\mathbf{U}_c = \min\left(c_\alpha |\mathbf{v}|, \max\left(|\mathbf{v}| \right) \right) \frac{\nabla \gamma}{|\nabla \gamma|}, \tag{12}$$

where c_α is the interface compression coefficient which controls the degree of interface compression (0 = no interface compression).

The modified VOF equation for sediment-laden free surface flow is given by (detailed derivation can be found in Appendix A):

$$\frac{\partial \alpha_w}{\partial t} + \nabla\bullet\left(\alpha_w \mathbf{v}\right) + \nabla\bullet\left[\alpha_w\left(-\frac{\alpha_s}{\gamma} - \frac{\alpha_w \alpha_s\left(\rho_s - \rho_w\right)}{\rho} + \frac{\alpha_a \alpha_w \alpha_s\left(1-S\right)}{\gamma\left(\alpha_w + \alpha_s S\right)}\right)\mathbf{w}\right], \qquad (13)$$
$$+\nabla\bullet\left(\alpha_w \alpha_a \mathbf{U}_c\right) = 0$$

where the 2nd term represents the water volumetric flux due to the averaged mixture velocity. The 3rd term represents the relative water flux due to slip between sediment and water. This term ensures full coupling between the sediment and water conservation equations, i.e. any net sediment flux into a control volume will produce an equivalent water flux out of the control volume. The last term in Eq. (13) represents the interface compression flux which is only active on the water-air interface. This equation reduces to the standard VOF equation when the sediment volume fraction vanishes.

Finally, the momentum conservation equation for the 3-phase mixture can be obtained by taking the sum of Eq. (2) over all phases:

$$\frac{\partial \sum_k \alpha_k \rho_k \mathbf{v}_k}{\partial t} + \nabla\bullet\left(\sum_k \alpha_k \rho_k \mathbf{v}_k \mathbf{v}_k\right) = -\nabla\left(\sum_k \alpha_k p_k\right) + \nabla\bullet\left[\sum_k \alpha_k \left(\bar{\bar{\tau}}_k + \tau_k^T\right)\right] \qquad (14)$$
$$+\sum_k \alpha_k \rho_k \boldsymbol{g} + \sum_k \boldsymbol{M}_k$$

Using Eq. (4), the 1st term of LHS of Eq. (14) is reduced to $\rho \boldsymbol{v}$. The 2nd term represents the sum of advection flux for all phases which can be written in terms of the mixture advection flux and relative velocity as follows:

$$\sum_k \alpha_k \rho_k \mathbf{v}_k \mathbf{v}_k = \rho \mathbf{v}\mathbf{v} - \tau_{s\text{-}w}^D - \tau_{m\text{-}a}^D \qquad (15)$$

The last two terms in the RHS of Eq. (15) are coined "diffusion stresses". Where $\tau_{s\text{-}w}^D$ represents the additional momentum diffusion due to the slip velocity between sediment and water and $\tau_{m\text{-}a}^D$ is the additional momentum diffusion due to the relative velocity between sediment-water suspension and air. Those two terms are given, by definition, as (detailed derivation can be found in Appendix A):

$$\tau_{s\text{-}w}^D \equiv -\alpha_s\left(1 - \frac{\alpha_s}{\gamma}\right)\frac{\rho_s \rho_w}{\rho_m}\mathbf{w}\mathbf{w} \qquad \tau_{m\text{-}a}^D \equiv -\gamma \alpha_a \frac{\rho_a \rho_m}{\rho}\mathbf{U}_c \mathbf{U}_c\,, \qquad (16)$$

where ρ_m is the density of the water-sediment suspension and given by:

$$\rho_m = \frac{\alpha_s \rho_s + \alpha_w \rho_w}{\gamma} \qquad (17)$$

For the pressure term, the continuous phase (air and water) pressures are separated from the dispersed phase pressure because each one represents quite different physical phenomenon. So, the pressure term in Eq. (14) will be written as:

$$\sum_k \alpha_k p_k = \bar{\bar{p}} + p_s\,, \qquad (18)$$

where $\bar{\bar{p}}$ is the common pressure field shared by air and water, and p_s is the solid pressure which results from enduring contact and collision between particles. The

ACCEPTED MANUSCRIPT

ACCEPTED MANUSCRIPT

constitutive equation for this term is supplied in §3.1. The mixture body force is readily defined as:

$$\sum_k \alpha_k \rho_k \boldsymbol{g} = \rho \boldsymbol{g} \tag{19}$$

It is customary in OpenFOAM to combine the mixture (static) pressure and the body force (hydrostatic pressure gradient) into a new modified pressure term (p_{rgh}). This is numerically more efficient [75] and advantageous for the specification of the pressure at the boundaries of the domain [110].

$$\begin{aligned} & p_{rgh} \equiv \bar{\bar{p}} - \rho \boldsymbol{g} h \\ & \nabla p_{rgh} = \nabla\left(\bar{\bar{p}} - \rho \boldsymbol{g} h\right) = \nabla \bar{\bar{p}} - \nabla\left(\rho \boldsymbol{g} h\right) = \nabla \bar{\bar{p}} - \boldsymbol{g} h \nabla\left(\rho\right) - \rho \boldsymbol{g} \\ & -\nabla \bar{\bar{p}} + \rho \boldsymbol{g} = -\nabla p_{rgh} - \boldsymbol{g} h \nabla\left(\rho\right) \end{aligned} \tag{20}$$

The sum of viscous and turbulent stresses for all phases yields the mixture viscous and turbulent shear stress tensors, respectively:

$$\begin{aligned} & \sum_k \alpha_k \bar{\bar{\tau}}_k = \bar{\bar{\tau}} \\ & \sum_k \alpha_k \tau_k^T = \tau^T \end{aligned} \tag{21}$$

The mixture shear stress tensor contains the shear component of the particle-stress tensor, which will be described as an increase in the mixture viscosity as will be discussed in §3.2.

The mixture momentum transfer term is given by:

$$\sum_k \boldsymbol{M}_k \equiv \boldsymbol{M}_m \tag{22}$$

All the inter-phase forces that cause momentum transfer and appear in the individual phase momentum transfer term $\boldsymbol{M}_k$ (e.g. drag and lift) will cancel out when the sum is made over all phases, except the effect of the surface tension force [67]. Ishii and Hibiki [67] have derived an equation for the mixture momentum transfer term $\boldsymbol{M}_m$ which exactly matches the equation provided by the continuum surface force (CSF) model of Brackbill [18]:

$$\boldsymbol{M}_m = \boldsymbol{F}_\sigma = 2\sigma H \nabla \gamma, \tag{23}$$

where $\boldsymbol{\sigma}$ is the surface tension coefficient and H is the mean interface curvature which is given as:

$$2H = \nabla \bullet \boldsymbol{n} = -\nabla \bullet \frac{\nabla \gamma}{\left|\nabla \gamma\right|}, \tag{24}$$

where $\boldsymbol{n}$ is the unit normal vector of the interface pointing out from water into air. In Eq. (23) the surface tension coefficient is assumed to be constant. It is clear from this equation that the surface tension will be only active at the free surface (water-air interface) which is the only location where $\nabla \gamma$ is nonzero.

The final form of the 3-phase momentum conservation equation is given by:

ACCEPTED MANUSCRIPT

$$\frac{\partial \rho \mathbf{v}}{\partial t} + \nabla \bullet \left(\rho \mathbf{v}\mathbf{v} \right) = -\nabla \left(p_{rgh} + p_s \right) + \nabla \bullet \left[\bar{\bar{\tau}} + \tau^T + \tau^D_{s\text{-}w} + \tau^D_{m\text{-}a} \right] - \boldsymbol{g} h \nabla \left(\rho \right) + 2\sigma H \nabla \gamma \quad (25)$$

3. Closures and constitutive equations

The mathematical model of three-phase flow represented in the form of system equations shown in §2 is not complete since the number of unknowns is more than the number of equations. So, supplementary constitutive equations have to be provided to close this system of equations.

Essentially, constitutive equations are needed for: particle stresses, the viscous stress tensor, mixture viscosity, the turbulent stress tensor, relative velocities and drag coefficient.

3.1 Particle stresses

As in fluids, the particle stress tensor usually is decomposed into particle normal stress or particle pressure (p_s) and particle shear or deviatoric stress tensor (τ_s).

According to Johnson and Jackson [76], particle or solid phase stresses in dense suspensions arise mainly as a result of momentum transfer due to the contact forces (collision and friction). Thus, both particle pressure and particle shear stress should have a collisional component and a frictional component. Two approaches are usually used to obtain the required closures for particle stresses: kinetic theory for granular flow (KTGF) [73, 93, 111] and dense granular flow rheology [53, 97].

KTGF provides a set of constitutive equations which links the macroscopic (averaged) flow quantities such as solids particle pressure, shear stress tensor and viscosity to the microscopic physics. Microscopic behavior is described in terms of particle volume fraction, restitution coefficient and the so-called granular temperature which represents a measure of the kinetic energy of particles fluctuations. This is in analogy with the kinetic theory of gases in which the temperature is a measure of the kinetic energy of the random motion. The main difference between KTGF and the classical kinetic theory of gases is that in case of granular flow part of the kinetic energy is lost during collisions (inelastic collision)[76]. This is taken into account in KTGF by the restitution coefficient which is a measure of the ratio between the velocities before and after collisions [53].

Since it has a strong impact on the momentum equation, a PDE for the balance and time evolution of the granular temperature must be solved and coupled with the momentum equation. This makes sediment transport models based on the KTGF computationally intensive.

Originally, it had a very narrow application limit since it is only valid when the collisions are uncorrelated, instantaneous and binary, a situation that can only be fulfilled in a dilute regime [71]. Recently, KTGF has made important progress by extending its applicability to dense concentration conditions [10]. Currently, velocity correlations [72], friction effects [12] and particle stiffness [11] can be taken into account. However, the differences between theory, applications in discrete element method (DEM) models and measurements still show significant discrepancies, even for monodisperse spherical particles, which requires to be resolved before it can be used in applications with poly-

dispersed natural sediments. Validation of KTGF against new flume experiments by Matoušek & Zrostlik [96] showed disagreement for particle volume fractions above 0.47.

Kamrin & Koval [79] propose a nonlocal fluidity (i.e. inverse viscosity) relation for flowing granular materials as an alternative for kinetic theory. The granular fluidity is defined in analogy of the inverse viscosity of a yields stress fluid as $G = \dot{\gamma} / \mu$. Disagreement with KTGF was found for volume fractions above 0.57 [132].

In the current study, the more widely implemented dense granular flow rheology or $\mu(I)$ rheology is adopted to obtain the particle stresses between grains in mutual contact. This is a phenomenological approach based on experimental results [97] and dimensional analysis [17]. This approach was used as a successful alternative of the KTGF by several researchers [29, 89, 106]. The particle pressure is addressed first. It is decomposed into two components:

$$p_s = p_s^f + p_s^k , \tag{26}$$

where p_s^f is the enduring contact component (equivalent to the effective stress in soil mechanics), and p_s^k is the kinetic or dynamic component. The original terminology [76] for the first term as the "frictional" component refers to the static friction angle and not to frictional motion. Likewise, it is misleading to keep the original term "collisional" component for the second, since the dynamic interaction may be both collisional and/or frictional.

Here, we start from the same closures as those utilized in sedFoam [28]. The empirical closure of Johnson and Jackson [76] is used to calculate p_s^f :

$$p_s^f = \begin{cases} C_p \dfrac{\left(\alpha_s - \alpha_{\min}^{fric}\right)^{C_1}}{\left(\alpha_{\max} - \alpha_s\right)^{C_2}} & \alpha_s \geq \alpha_{\min}^{fric} \\ 0 & \alpha_s < \alpha_{\min}^{fric} \end{cases}, \tag{27}$$

where C_p , C_1 and C_2 are empirical constants, equal to 0.05, 3 and 5, respectively [77]. $\alpha_{\min}^{fric}$ is the critical minimal volume fraction at which the persisting contact mechanism becomes significant. From the knowledge of possible packing sequences for monodisperse spherical particles [124] it is to be expected that $0.524 < \alpha_{\min}^{fric} < 0.605$, where the lower limit is given by the primitive or simple cubic packing fraction, i.e. $\pi / 6$, and the upper limit is the more stable hexagonal packing fraction, i.e. $\pi / 3^{3/2} = 0.6046$. Similarly, $0.64 < \alpha_{\max} < 0.74$, where the lower limit corresponds to the random close packing fraction[69], and the upper limit to the closest packing, i.e. $\pi / 3\sqrt{2}$. Simulations with granular fluidity theory yields a critical volume fraction of 0.57 [132]. DEM simulations indicate that the critical volume fraction varies from 0.58 to 0.64 [37]. These packing fractions also increase with polydispersity [20], which has to be taken into account for natural sediments.

The closure for the dynamic component of the particles pressure is regime dependent. A flow regime is defined as viscous or inertial based on the Stokes number

ACCEPTED MANUSCRIPT

$St_g = d_p\sqrt{\rho_s p_s^k} / \mu_f$ [23]. Chauchat et al. [29] modified the empirical equation of Boyer [17] to develop an expression for p_s^k. In the viscous regime (St_g <1.0) this is given by:

$$p_s^k = \mu_f \left(\frac{B_\phi \alpha_s}{\alpha_{\max} - \alpha_s} \right)^2 \|\boldsymbol{D}\| \tag{28}$$

And for the inertial regime (St_g >1.0), p_s^k is given by:

$$p_s^k = d_p^2 \rho_s \left(\frac{B_\phi \alpha_s}{\alpha_{\max} - \alpha_s} \right)^2 \|\boldsymbol{D}\|^2, \tag{29}$$

where B_ϕ is dilatancy parameter, and **D** is the deviatoric part of the strain rate tensor, given by:

$$\boldsymbol{D} = \boldsymbol{S} - \frac{1}{3} tr(\boldsymbol{S})\boldsymbol{I} = \boldsymbol{S} - \frac{1}{3}(\nabla.\mathbf{v})\boldsymbol{I} = \frac{1}{2}\left(\nabla\mathbf{v} + (\nabla\mathbf{v})^T - \frac{2}{3}(\nabla.\mathbf{v})\boldsymbol{I} \right) \tag{30}$$

It can be seen that p_s^k scales linearly and quadratically with the strain rate in the viscous and inertial regime, respectively. This is in agreement with the findings of Bagnold [7]. Moreover, it can be seen that the enduring contact component of the normal stress is shear-rate independent, which confirms that this component is important to model the quasi-static bed layer.

In dense granular flow rheology, the particle shear stress is defined as [78]:

$$\boldsymbol{\tau}_s = \mu(I) p_s \frac{\boldsymbol{D}}{\|\boldsymbol{D}\|} \tag{31}$$

Equation (31) is analogous to the equation of dynamic friction between two solids. So, $\mu(I)$ is the dynamic friction coefficient that relates the particle shear stress to the particle normal stress (pressure). $\mu(I)$ is a function of the dimensionless control parameter *I*. The definition of this parameter and the form of $\mu(I)$ is also regime dependent.

In the viscous regime (St_g <1.0) the control parameter is the viscous number I_v :

$$I_v = \frac{\mu_f}{p_s} \|\boldsymbol{D}\| \tag{32}$$

and $\mu(I_v)$ is given by:

$$\mu(I_v) = \mu_s + \frac{\mu_2 - \mu_s}{I_0 / I_v + 1}, \tag{33}$$

where μ_s is the static friction coefficient, which usually is taken equal to the tangent of the angle of repose, μ_2 is called the dynamical friction coefficient and I_0 is an empirical rheological coefficient [31]. For the viscous regime, the constants in equation (33) are

ACCEPTED MANUSCRIPT

given by Boyer et al. [17] for neutrally buoyant beads as: $\mu_s = 0.32$, $\mu_2 = 0.7$, $I_0 = 0.005$. Houssais et al. [62] found the same values valid for spherical acrylic particles except for $I_0 = 0.001$.

In the inertial regime ($St_g > 1.0$): the control parameter is the inertial number I:

$$I = d_p \sqrt{\frac{\rho_s}{p_s}} \|\boldsymbol{D}\| \tag{34}$$

and $\mu(I)$ is given by:

$$\mu(I) = \mu_s + \frac{\mu_2 - \mu_s}{I_0 / I + 1}, \tag{35}$$

where for glass beads in air: $\mu_s = 0.38$, $\mu_2 = 0.64$, $I_0 = 0.3$ [78]. Substituting Eq. (33) or (35) into Eq. (31), we get the following form of particle shear stress:

$$\boldsymbol{\tau}_s = \left(\mu_s + \frac{\mu_2 - \mu_s}{I_0 / I_v + 1} \right) p_s \frac{\boldsymbol{D}}{\|\boldsymbol{D}\|} \tag{36}$$

The 1st term in Eq. (36) corresponds to the yield stress at which the transition from a quasi-static bed to the liquid regime takes place. This yield stress is a function of the solid phase pressure, angle of repose and volume fraction. While the 2nd term can be seen as a non-Newtonian contribution to the particle shear stress [31].

Equation (36) cannot be used to solve the problem when sediment packing occurs or when the quasi-static bed is included within the domain because in this case $\|\boldsymbol{D}\|$ will be zero in the bed layer, which will cause numerical instabilities. To overcome this difficulty, first the particle phase viscosity, μ_p, is derived from Eq. (36) with the help of Newton's law of viscosity:

$$\boldsymbol{\tau}_s = \mu(I) p_s \frac{\boldsymbol{D}}{\|\boldsymbol{D}\|} = 2\mu_p \boldsymbol{D} \quad \Rightarrow \quad \mu_p = \frac{\mu(I) p_s}{2\|\boldsymbol{D}\|} \tag{37}$$

Equation (37) suffers from the same shortcoming. To solve that, a so-called "Regularization" procedure must be used. In the literature, there are many types of this regularization, e.g. [9, 54, 102]. In this study the regularization proposed by Chauchat [31] based on Bercovier regularization [9] is used and adapted for $\mu(I)$ rheology:

$$\mu_p = \frac{\mu(I) p_s}{\left(\|\boldsymbol{D}\|^2 + \lambda_r^2 \right)^{0.5}}, \tag{38}$$

where λ_r is the regularization parameter, which is used to avoid division by zero. However, it should be taken very small to reduce the smearing of the stress-rate of strain curve. The particle viscosity given by Eq. (38) will be used in the mixture shear stress tensor discussed in the following section.

ACCEPTED MANUSCRIPT

ACCEPTED MANUSCRIPT

3.2 Viscous stress tensor

The averaged mixture shear stress tensor in the momentum equation is defined as:

$$\overline{\overline{\tau}} \equiv \sum_k \alpha_k \overline{\overline{\tau}}_k = \alpha_s \overline{\overline{\tau}}_s + \alpha_w \overline{\overline{\tau}}_w + \alpha_a \overline{\overline{\tau}}_a \tag{39}$$

It is evident from Eq. (39) that many complicated mechanisms have pervaded $\overline{\overline{\tau}}$. This term accounts for the averaged shear stress in water, sediment and air, which arises due to different mechanisms in each case. According to Bird et al. [14], those individual shear stress tensors can be substituted by a hypothetical mixture shear stress tensor using the generalized Newton's fluid constitutive equation. In order to do that, an effective viscosity and averaged velocity fields must be introduced. So following that, the averaged mixture shear stress tensor can be written as:

$$\overline{\overline{\tau}} = \mu_{eff} \left(\nabla \mathbf{v} + (\nabla \mathbf{v})^T - \frac{2}{3} (\nabla . \mathbf{v}) \boldsymbol{I} \right), \tag{40}$$

where μ_{eff} is the effective mixture dynamic viscosity, given by:

$$\mu_{eff} = \gamma \left(\mu_p + \mu_m \right) + (1 - \gamma) \mu_a , \tag{41}$$

where μ_p is the particle phase viscosity defined by Eq. (38), and μ_a is the air viscosity.

μ_m is the mixture or suspension viscosity which represents the modified water viscosity due to the presence of solid particles. When solid particles are added to water to form a suspension, additional forces arise between solid particles and fluid. Those forces represent new momentum transfer mechanisms which in turn are expected to increase the suspension viscosity. These forces or interactions include hydrodynamic forces (e.g. drag and lift), colloidal forces and particle-particle contact forces [32].

There are many suspension viscosity closures that can be found in the literature, see e.g. [98, 127]. Frequently used closures include Einstein [47], Batchelor & Green [8], Krieger and Dougherty [83], and Thomas [117]among others. In the present model, most of these formulae have been implemented. The suspension viscosity in those closures is given as a function of particle volume fraction and, sometimes, the packing limit. Only the latter is suitable for non-dilute conditions. For example, the Krieger and Dougherty mixture viscosity is given by:

$$\mu_m = \mu_f \left(1 - \frac{\alpha_s}{\alpha_{max}} \right)^{-B_E \alpha_{max}} , \tag{42}$$

where B_E is called the Einstein coefficient and usually taken = 2.5.

3.3 Relative velocities

It is now evident that the relative velocity between water and sediment plays an important role in our multiphase model. It is required in the mass conservation equations for sediment and water to model the relative sediment flux. This flux is crucial to model both erosion and sedimentation processes. In addition, the diffusion stress in the momentum equation is also a function of the relative velocity.

The relative velocity arises mainly due to the inertial effect which in turn is controlled by the particle-fluid density ratio. In addition to this effect, in the current study, two ad-

ditional contributions to the relative velocity are considered, namely: the turbulent dispersion force and the shear-induced self-diffusion. Hence, the relative velocity in the current model consists of 3 contributions:

$$\mathbf{w} = \mathbf{w}_i + \mathbf{w}_{td} + \mathbf{w}_{sd} \tag{43}$$

The derivation of the relative velocity closure follows Manninen & Taivassalo [94]. Their main assumption is that "*a local equilibrium between the phases is reached over a short spatial length scale*". Manninen & Taivassalo started the derivation by combining the momentum equations for the particle and the mixture, and using a momentum transfer term as a function of drag force only, the following closure for relative velocity due to inertial effect was introduced:

$$\mathbf{w}_i = \frac{4}{3}\frac{d_p^2\left(\rho_s - \rho\right)}{\mu_f C_d Re_p}\left[\boldsymbol{g} - (\mathbf{v}.\nabla)\mathbf{v} - \frac{\partial \mathbf{v}}{\partial t}\right], \tag{44}$$

where d_p is the sediment particle diameter, C_d is the drag coefficient and $Re_p = d_p|\mathbf{w}|/\upsilon_f$ is particle Reynolds number. The last term in Eq. (44) represents the mixture acceleration. Actually, Eq. (44) is nothing else than the definition of a drag force on a particle subject to a combined acceleration field of gravity and water motion.

The drag coefficient for a particle in clear water or a dense suspension has been extensively reviewed in many previous studies, e.g. [110, 127]. In the present model, many drag coefficient formulas for dense suspension have been implemented, e.g. Wallis [123], Andersson [4] and Rusche [110]. In those formulae the drag coefficient is given as a function of the clear water drag C_{d0} and the particle volume fraction, e.g. the Wallis drag function is given by:

$$\begin{aligned} C_d &= C_{d0}(1-\alpha_s)^{3-2n} \\ n &= 4.7\frac{1+0.15Re_p^{0.687}}{1+0.253Re_p^{0.687}} \end{aligned} \tag{45}$$

In turbulent flow, when averaging the instantaneous turbulent drag, two forces arise, namely the mean drag force which represents the mean momentum transfer between water and sediment, and the turbulent dispersion force which accounts for the diffusion of sediment particles into water due to turbulent fluctuations. In the derivation of Eq. (44), Manninen & Taivassalo only considered the drag force due to the mean relative velocity. So, an additional term should be added to the relative velocity closure to account for the turbulent dispersion. In the present study, the closure provided by Deutsch and Simonin [41]is used:

$$\mathbf{w}_{td} = -\frac{\nu_t}{Sc_t}\left(\frac{\nabla\alpha_s}{\alpha_s} - \frac{\nabla\alpha_w}{\alpha_w}\right), \tag{46}$$

where ν_t and Sc_t are the eddy viscosity and turbulent Schmidt number, respectively.

In addition to particle inertia and the turbulent dispersion force, a slip velocity between particle and fluid may arise due to shear-induced self-diffusion. This mechanism takes place when hindered particles in a dense suspension are forced to flow. Single particles

ACCEPTED MANUSCRIPT

try to follow the flow, but they are confronted by either slower or faster particles on their way. This forces those particles to deviate from their original streamline. As a result, they will exhibit fluctuating motion as they move. Those fluctuations of individual particles are of diffusive nature when viewed over a long enough timescale [19]. Shear-induced self-diffusion was found to be a more significant diffusion mechanism when the particle size increases [46].

Gadala-Maria[55] found that the resuspension of a settled layer of sediment can take place not only due to turbulence but can also occur in viscous conditions. Leighton and Acrivos [91] have shown that this viscous resuspension can be described as shear-induced self-diffusion.

The contribution to the slip velocity due to shear-induced self-diffusion is given by Zhang [131] and adapted for a 3-phase mixture:

$$\mathbf{w}_{sd} = -0.15\left(d_p \frac{\alpha_s}{\gamma}\right)^2 \nabla\dot{\gamma}, \tag{47}$$

where $\dot{\gamma} = \sqrt{2\boldsymbol{D} : \boldsymbol{D}}$ is the scalar shear rate or shear rate intensity.

3.4 Turbulent stress tensor

The mixture turbulent stress tensor is defined as:

$$\tau^T = \sum_k \alpha_k \tau_k^T = \sum_k \alpha_k \overline{\overline{\rho_k \mathbf{v}'_k \mathbf{v}'_k}} \tag{48}$$

This term is usually modeled using the Boussinesq eddy viscosity hypothesis as:

$$\tau^T = \mu_t \left(\nabla\mathbf{v} + (\nabla\mathbf{v})^T - \frac{2}{3}(\nabla.\mathbf{v})\boldsymbol{I}\right) - \frac{2}{3}\rho k \delta_{ij}, \tag{49}$$

where μ_t is the dynamic eddy viscosity, k is the turbulent kinetic energy (TKE) per unit mass, and δ_{ij} is the Kronecker delta. The main task here is to find a suitable closure for μ_t.

The choice of an appropriate turbulence model is crucial in sediment-laden flow simulation. An appropriate model should contain the required damping functions to model the turbulence damping in the near-bed layer due to the presence of particles and due to the discontinuity in density at the free surface.

In the current study, two turbulence models are tested in different cases, the two-phase mixing length model of Li and Sawamoto [92] and a modified version of the standard k-ε model [87] adapted for sediment transport problems at high phase fraction.

In the two-phase mixing length model, the eddy viscosity is given by:

$$\mu_t = \rho l_m^2 \left\|\nabla\mathbf{v}\right\|, \tag{50}$$

where l_m is the mixing length, which is given by:

$$l_m = k\int_0^z 1 - \left(\frac{\alpha(\xi)}{\alpha_{max}}\right)^e d\xi, \tag{51}$$

ACCEPTED MANUSCRIPT

where k is the von Karman constant and e is a calibration exponent. This model is valid for 1DV cases only. The numerical implementation of the two-phase mixing length model which was made available in the distribution of sedFoam 2.0 [28] is used in the 1DV validation case in the current study.

For 2D and 3D cases, a modified version of the k-ε model (hereinafter mixture k-ε model) is used. The modified version contains two additional terms in both the k and ε equations to account for turbulence damping due to the presence of particles. The 1st term accounts for the buoyancy production/destruction of TKE due to the density gradient which in turn can be a result of a volume fraction gradient or temperature gradient [107]. The 2nd term represents the turbulence damping due to drag.

In this model, the eddy viscosity is given by:

$$\mu_t = \rho C_\mu \frac{k^2}{\varepsilon}, \tag{52}$$

where C_μ is an empirical model coefficient (see Table 1), k is the TKE, and ε is the rate of dissipation of TKE. The modified balance equations of k is given by:

$$\frac{\partial \rho k}{\partial t} + \nabla \bullet \left(\rho \boldsymbol{v} k \right) = \nabla \bullet \left[\left(\mu_m + \frac{\mu_t}{\sigma_k} \right) \nabla k \right] + 2\mu_t \boldsymbol{D} : \boldsymbol{D} - \rho\varepsilon - G_k - D_k, \tag{53}$$

where G_k represents the buoyancy production/destruction of TKE and is given by Henkes et al. [57]:

$$G_k = \gamma C_g \upsilon_t \left(\boldsymbol{g} \bullet \nabla \rho \right) = \gamma C_g C_\mu \frac{k}{\varepsilon} \left(\boldsymbol{g} \bullet \nabla \rho \right) k = G_{coeff} .k, \tag{54}$$

where C_g is the reciprocal of turbulent Schmidt number. D_k is the drag-induced turbulence damping term and is given by Hsu et al. [63]:

$$D_k = 1.5 C_d \frac{\rho_w}{d_p} |\mathbf{w}| (1 - t_{mf}) \alpha_s k = D_{coeff} .k, \tag{55}$$

where the parameter t_{mf} represents the degree of correlation between the particle and fluid fluctuations. This parameter is given by:

$$t_{mf} = e^{-B.St}, \tag{56}$$

where B is an empirical model coefficient and St is the Stokes number, given by:

$$St = \frac{t_p}{t_l}, \tag{57}$$

where t_p and t_l are the particle response time and fluid characteristic time scale, respectively, and given by:

$$t_p = \frac{\rho_s d_p}{0.75 C_d \rho_w |\mathbf{w}| \alpha_w} \tag{58}$$

ACCEPTED MANUSCRIPT

$$t_l = \frac{k}{6\varepsilon} \tag{59}$$

The modified balance equation of ε is given by:

$$\frac{\partial \rho\varepsilon}{\partial t} + \nabla\bullet\left(\rho \boldsymbol{v}\,\varepsilon\right) = \nabla\bullet\left[\left(\mu_m + \frac{\mu_t}{\sigma_\epsilon}\right)\nabla\varepsilon\right] + C_{1\epsilon}\frac{\varepsilon}{k}2\mu_t \boldsymbol{D}:\boldsymbol{D} - C_{2\epsilon}\rho\frac{\varepsilon^2}{k} - C_{1\epsilon}G_{coeff}\tanh\left(\frac{\left\|\mathbf{v}_g\right\|}{\left\|\mathbf{v}-\mathbf{v}_g\right\|}\right)\varepsilon - C_{3\epsilon}D_{coeff}\,\varepsilon \tag{60}$$

where $\mathbf{v}_g$ is velocity component in the direction of gravity, and given by:

$$\mathbf{v}_g = \left(\frac{\boldsymbol{g}}{\|\boldsymbol{g}\|}\bullet\mathbf{v}\right)\frac{\boldsymbol{g}}{\|\boldsymbol{g}\|} \tag{61}$$

σ_k, σ_ϵ, $C_{1\epsilon}$, $C_{2\epsilon}$, and C_g are empirical model coefficients and their default values are given in Table 1.

The numerical implementation of the mixture k-ε model is based on the buoyant k-ε model which is distributed as a part of the standard OpenFOAM library [126] and contains the buoyancy destruction term only. In the current study this model was used as a base class for the mixture k-ε model in which the additional drag-induced damping term was added.

This model is still a simplification of the complete TKE balance for suspension flow [50]. Therefore the present model will have to be extended in the future to account for additional particle-turbulence mechanisms which become important in non-dilute conditions.

Table 1. Default values of mixture *k-ε* model coefficients [107]

C_μ	σ_k	σ_ϵ	$C_{1\epsilon}$	$C_{2\epsilon}$	$C_{3\epsilon}$	C_g
0.09	1.0	1.30	1.44	1.92	1.20	1.43

4. Numerical Implementation

In the current study OpenFOAM [126], an open source 3D finite volume toolbox, is used to solve the system of partial differential equations and the closures presented in §2 and §3. OpenFOAM contains the required infrastructure to discretize and solve continuum mechanics PDEs based on the Finite Volume Method (FVM). This includes various numerical schemes for temporal and spatial derivatives discretization, standard libraries for turbulence and viscosity models, and different solution algorithms.

However, special attention should be paid in the current study mainly because:

1. The new set of equations contains several additional terms when compared to the standard counterpart, which sometimes needs special treatment.

ACCEPTED MANUSCRIPT

ACCEPTED MANUSCRIPT

2. Several closures need to be coupled with the main governing equations. For instance the coupling between relative velocity closure, sediment mass conservation equation, and the granular rheology closures.
3. The numerical instabilities that can arise when the sediment volume fraction reach (or exceeds) the maximum packing limit.

In the current study, the standard PIMPLE algorithm in OpenFOAM has been modified to tackle these challenges. A simple illustration of the modified solution algorithm is shown in Figure 1.

The calculations start by computing the relative velocities according to Eq. (43). Then, the sediment and water mass conservation equations [Eq. (10) and (13)] are solved several times (usually twice) within a correction loop to guarantee coupling between the water and sediment phase fractions, i.e. they must sum to 1.0 in the absence of air.

The water mass conservation equation is solved using the MULES (Multidimensional Universal Limiter for Explicit Solution) algorithm implemented in OpenFOAM [39, 110, 125] and based on the idea of the Flux-Corrected Transport (FCT) algorithm [130]. This treatment is essential to guarantee the boundedness of the water phase fraction while keeping the numerical diffusion and interface smearing to the minimum.

To discretize the sediment mass conservation equation, a fully implicit time scheme was used. For the advection term, either a 2nd order linear scheme or a limited linear scheme, in case of undergoing an unbounded solution, was used without using the MULES algorithm. This treatment was found to be accurate enough and reduced the computational cost.

After obtaining the phase fraction of all phases, the granular rheology closures are solved to obtain the particle pressure and the particle viscosity. In this step, it was inevitable to limit the values of the particle viscosity to avoid numerical instabilities when the phase fraction is equal or slightly greater than the maximum packing limit.

The next step is to solve the momentum equation to obtain the mixture velocity field. In this step the pressure and flux fields from the previous time step are used; thus this is called the velocity predictor step.

The next step is to solve for the pressure. The only candidate equation for this task is the continuity equation [Eq. (7) or (8)]. The problem is that pressure does not appear explicitly in those equations. This is the well-known pressure-velocity coupling problem in incompressible solvers [70, 75, 122].

To overcome this difficulty, the OpenFOAM standards of deriving a pressure equation using momentum and continuity equation [70] is followed. The idea is simply to use the momentum equation [Eq. (25)] in discrete form to derive an explicit expression for velocity as a function of pressure and source terms, then substitute this expression into the continuity equation [Eq. (8)] to obtain the pressure equation. The resulting pressure equation in our case is similar to the pressure equation used in OpenFOAM standard solvers but contains some additional terms. It is given by:

$$\nabla\cdot\left(\frac{\nabla p_{rgh}}{\mathrm{a_P}}\right)=\nabla\cdot\left(\frac{\boldsymbol{H}(\mathbf{v})}{\mathrm{a_P}}-\frac{\boldsymbol{g}h\nabla(\rho)_p}{\mathrm{a_P}}-\frac{\nabla p_s}{\mathrm{a_P}}+\frac{2\sigma H\nabla\gamma}{\mathrm{a_P}}-\frac{\alpha_w\alpha_s(\rho_s-\rho_w)}{\rho}\mathbf{w}\right), \tag{62}$$

where $\boldsymbol{H}(\mathrm{v})$ represents the off-diagonal part of the matrix of the coefficients multiplied by the velocity. For more details about this procedure, the reader can refer to Jasak [70].

After Eq. (62) is solved, an updated pressure field is obtained which can be used to correct the velocity and flux fields. This step (pressure updating followed by velocity correction) is repeated several times to obtain consistent velocity-pressure fields.

Finally, the turbulence closure is solved and the mixture density and viscosity are updated. Optionally, the nonlinear terms in all system equations can be updated and solve the equations again. This, in one hand, increases the computational cost, but on the other hand enhances the stability and hence allows for a larger time step.

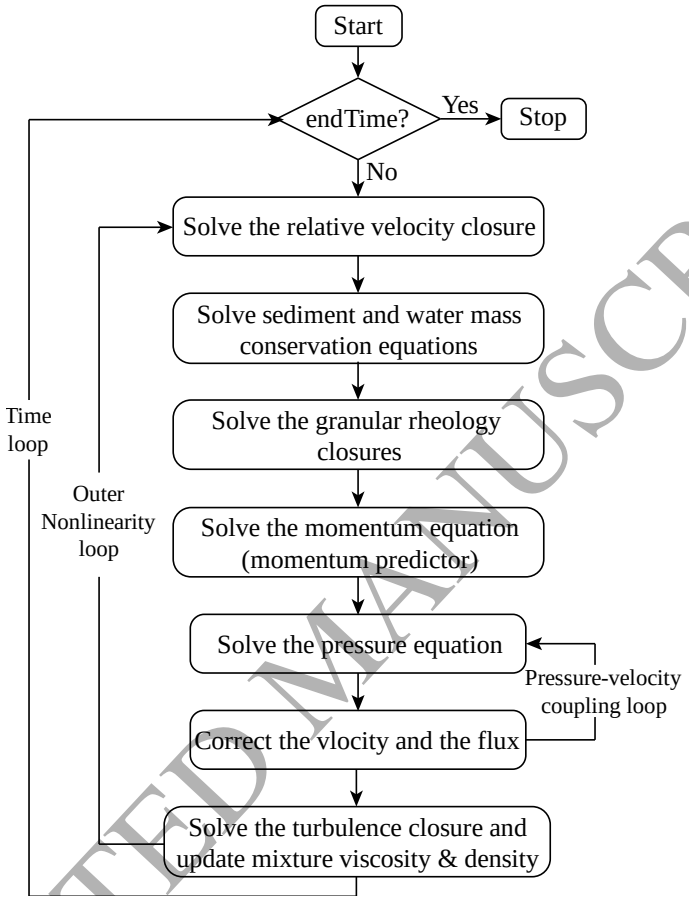


Figure 1: Flowchart of numerical solution of three phase sediment transport mixture

ACCEPTED MANUSCRIPT

ACCEPTED MANUSCRIPT

5. Model validation and test cases

To check the validity of the current numerical implementation, the model was tested against some experimental data sets. Those test cases were chosen to represent sediment transport in different modes. The complexity gradually increases from a simple sedimentation test in the 1st case to turbulent sheet flow and scour due to a horizontal submerged jet in the 3rd and 4th cases, respectively. A laminar bedload transport test case, for which an analytical solution exists, was used to validate the numerical implementation of the granular rheology closures. Finally, the wave-induced scour under a submarine pipeline was modeled to assess the model's capability to account for the interaction between free surface and sediment dynamics. In addition to model validation, those cases help in identifying the model sensitivity to the choice of the empirical model parameters and also the calibration of some of them.

It is worth mentioning that the input files (mesh, boundary conditions and initial conditions) used in the setup of the 1D test cases in the current study (sedimentation, laminar bedload and turbulent sheet flow) were obtained from the distribution of sedFoam 2.0 [28] which was made available as an open source.

5.1 Sedimentation of non-cohesive particles

The process of particle sedimentation represents one of the main processes that contribute to sand transport. So, any sand transport model must be able to reproduce this fundamental process accurately. To obtain this objective, the model should be able to calculate the particle settling velocity accurately taking into account the hindrance effect due to interference and collision between particles when the sediment volume fraction increases. In the current model, this boils down to choosing of a proper drag model.

In this section, the experimental data set from Van Bang et al. [121] is used to test the capability of the current model to reproduce the correct settling velocity and to assess the performance and calibrate the implemented drag model.

In this experiment, the settling of initially suspended non-cohesive particle in a fluid was monitored using an MRI device. The particles are mono-dispersed spherical polystyrene beads with diameter $d_p = 0.29 \pm 0.03$ mm and density $\rho_s = 1050$ kg/m^3. The carrier fluid is Rhodorsil silicone oil of density $\rho_f = 950$ kg/m^3 and viscosity $\nu_f = 2.01 \times 10^{-5}$ m^2/s. Initially, the particles were brought into suspension forming a well-mixed mixture of initial solid volume faction $\alpha_s = 0.50$. Then, the suspension was left to settle under gravity, and vertical concentration profiles were measured over time using a proton MRI device with a vertical resolution of 1.0 mm and temporal resolution of 0.16 Hz [29].

The numerical setup consists of a 1D mesh with vertical resolution $\Delta z = 0.3$ mm and time resolution $\Delta t = 10^{-3}$ s. In the current setup, the solution of the fluid mass conservation equation was turned off to reduce the computational cost and because the free surface effect on the sedimentation is expected to be insignificant. For the particle mass conservation equation, an implicit time scheme and a limited linear advection scheme were used. The limited scheme was used because the linear scheme causes a large overshoot of volume fraction at the upper water-sediment interface.

For the suspension viscosity, the Krieger and Dougherty closure [Eq. (42)] was selected in this case. For the drag closure, the Wallis model [Eq. (45)] was initially tested. However, it was found that this model underestimates the settling velocity. The model was

then modified by using a constant exponent (n) instead of variable exponent as a function of Re. The constant exponent was then calibrated and the best fit with experimental data was obtained for n = 3.10. The rheological parameters used in this case are shown in Table 2.

α_{max}	α_{min}^{fric}	C_p	C_1	C_2	B_ϕ	λ_r	μ_s	μ_2	I_o
0.635	0.57	0.05	3.0	5.0	0.66	10^{-4}	0.40	0.9	0.6

Table 2: The rheological parameters for sedimentation test case

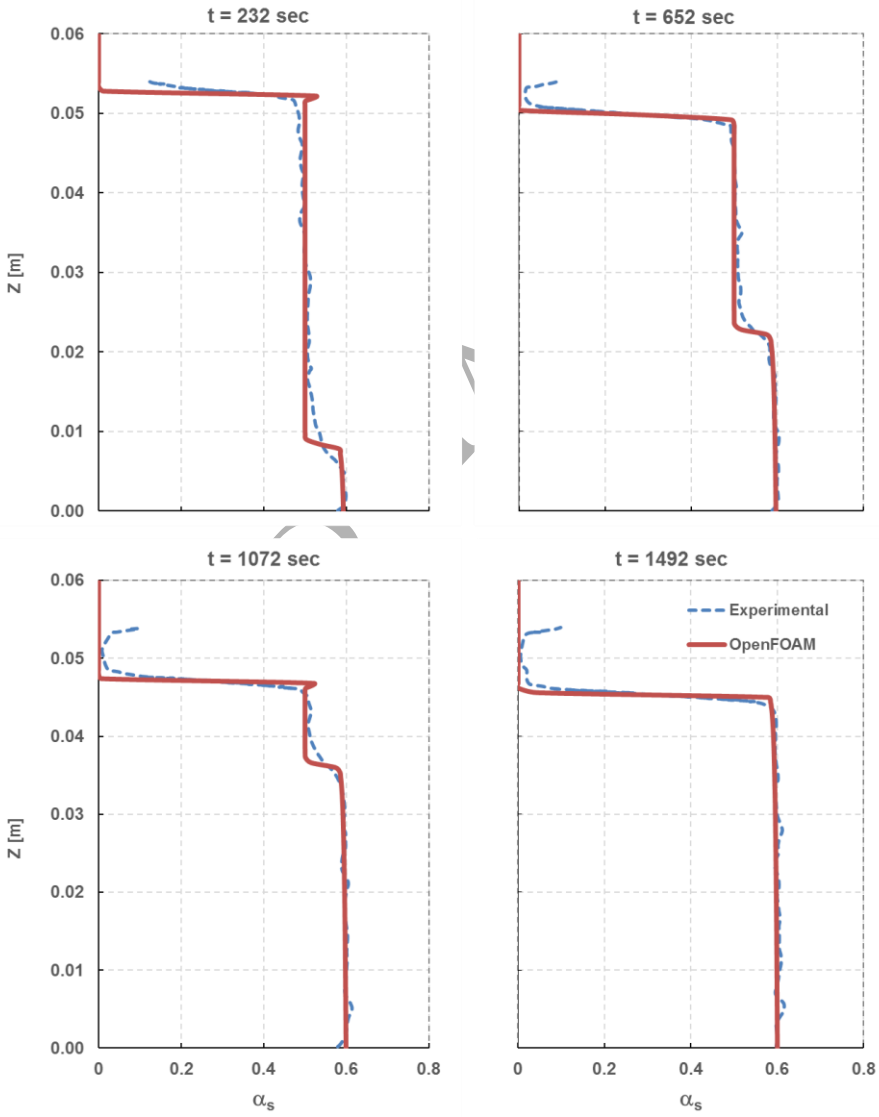


Figure 2: Comparison between sediment concentration profile from experimental data of Van Bang et al. [121] and the current numerical model results.

Figure 2 shows the results of the current numerical model as well as the corresponding experimental data for the particle concentration vertical profile at several time instanc-

es. Good agreement between the model results and the experimental data can be observed. The model was able to reproduce the correct concentration profile with a good estimate of the location of both upper interface between clear fluid and suspension, and the lower interface between suspension and packed bed, at all time instances. This implies the capability of the model to estimate the hindered settling velocity and the validity of the calibrated drag closure.

Figure 3 shows the sediment concentration and the particle pressure profiles at the end of simulation (after 30 minutes). The particle pressure obtained by the model is plotted against the theoretical value of the immersed sediment weight $\alpha_s(\rho_s - \rho_w)gh$ corresponding to the final concentration profile. This comparison shows a good agreement between the numerical model results and the theoretical value of particle pressure.

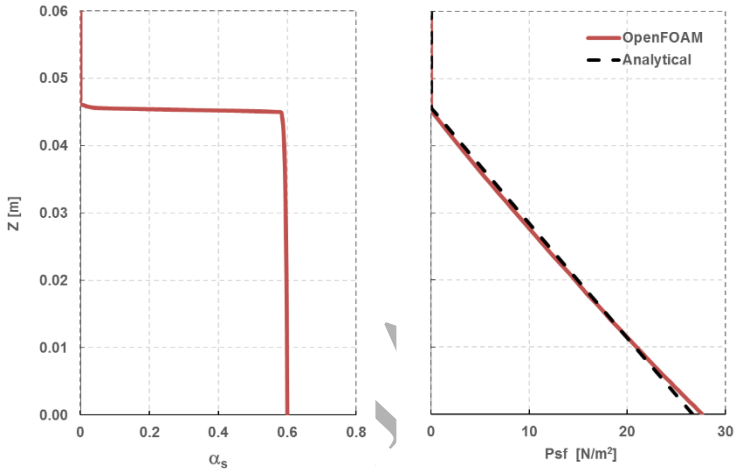


Figure 3: Sediment concentration profile (left) and particle stress profile plotted against immersed sediment weight (right) after 30 minutes of simulation time.

5.2 Laminar bedload transport

The dense granular flow rheology closures presented in §3.1 is a core model element. In order to check the correct numerical implementation of those closures, a test case for laminar bedload induced by Poiseuille flow of a Newtonian fluid over a granular flatbed was performed. For the flow and sediment transport conditions, an analytical solution is provided by Ouriemi et al. [101] in which the analytical solution was obtained using Einstein's correction for mixture viscosity and Coulomb rheology for sediment stresses. A script provided as a part of sedFoam 2.0 distribution [28] was used to compute this analytical solution for the sake of comparison with the current numerical model.

The numerical setup of this case consists of a 1D mesh with total height = 0.065 m. which is discretized uniformly into 200 cells. Particles of density $\rho_s = 1190$ kg/m^3 and diameter $d_p = 2$mm. are used. The carrier fluid density is $\rho_f = 1070$ kg/m^3 and its viscosity is $\nu_f = 2.52 \times 10^{-4}$ m^2/s. The flow was driven by a fixed mean pressure gradient = 100 kg/m^2.s^2 in the x-direction.

The Einstein mixture viscosity closure is used in the modeling of this test case. To model the Coulomb rheology used in the derivation of the analytical solution, simply $\mu_2 = \mu_s$ was set in equation (33) and the calculations of the kinetic pressure was turned off. The

ACCEPTED MANUSCRIPT

rest of the rheological parameters are shown in Table 3. The numerical discretization schemes are identical to the schemes used in the sedimentation test case. The free surface tracking was turned off and replaced by a zero velocity Dirichlet boundary condition at the top of the domain.

Comparison between the current numerical model results and the analytical solution of Ouriemi et al. [101] is shown in Figure 4 in terms of profiles of the sediment concentration, the streamwise velocity and the particle pressure. This comparison shows a good agreement between the model results and the analytical solution especially in terms of the particle pressure. This demonstrates that the granular rheology closures were correctly implemented. The slight discrepancy in terms of streamwise velocity may be attributed to the difference between the analytical and numerical sediment concentration profiles. In the analytical solution this profile was imposed as a step function while in the current model this is, obviously, one of the model outputs.

Since the analytical solution is only available for Coulomb rheology, additional comparison for the same test case was performed against the results of the numerical model of Aussillous et al. [5]. In this case, the model parameters remain the same with only one difference, namely the value of μ_2 which was taken = 0.94 in order to model the viscous granular flow regime (see Table 3). The results of this comparison are also shown in Figure 4. Very good agreement between the current numerical model and the numerical model of Aussillous et al. can be seen in this comparison. This confirms the correct implementation of the granular rheology closures and its ability to predict the correct granular stresses in different regimes.

Rheology	α_{max}	α_{min}^{fric}	C_p	C_1	C_2	B_ϕ	λ_r	μ_s	μ_2	I_o
Coulomb	0.635	0.57	0.05	3.0	5.0	1.0	10^{-4}	0.32	0.32	0.0077
Viscous regime	0.635	0.57	0.05	3.0	5.0	1.0	10^{-4}	0.32	0.94	0.0077

Table 3: The rheological parameters for laminar bedload transport test case

5.3 Sediment transport under sheet-flow condition

Sheet flow is a mode of sediment transport which takes place under severe, high-energetic flow conditions, e.g. storm conditions, in the near-bed layer with a thickness which typically extends several times the particle diameter. Very high sediment concentrations and a relatively high sediment velocity within the sheet flow layer give rise to a large sediment transport rate which in turn may result in a significant change of bottom morphology over a short timescale. An obvious example of this process is the change in the beach profile during a storm in which a significant beach profile changes can take place within a few hours.

In the current study, the capability of the newly developed model to simulate sediment transport in sheet flow regime is tested. The dataset from Revil-Baudard et al. [105] was used for validation. In this experiment, sheet flow was induced by a unidirectional flow of mean velocity equal to 0.52 m/s in water of 0.17 m depth. Particles are non-spherical lightweight polymethyl methacrylate (PMMA) with diameter $d_p = 3.0 \pm 0.5$ mm and density $\rho_s = 1190$ kg/m^3. The carrier fluid is water of density $\rho_f = 1000$ kg/m^3 and viscosity $\nu_f = 10^{-6}$ m^2/s.

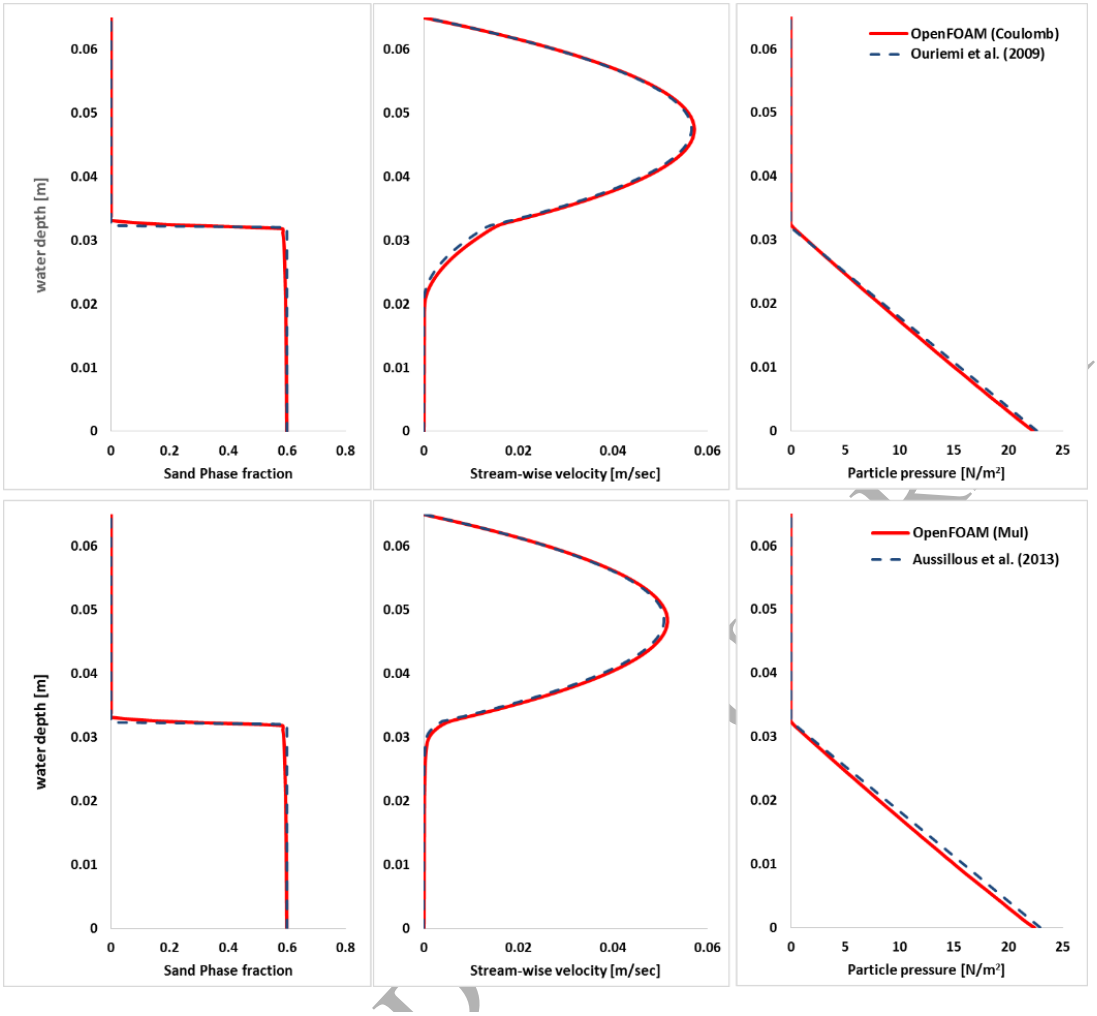


Figure 4: Comparison between the numerical model results for laminar bedload test case and the analytical solution of Ouriemi et al. [101] (upper panels) and numerical model of Aussillous et al. [5] (lower panels) in terms of sediment concentration profile (left), streamwise velocity (middle) and particle pressure (right)

An acoustic current and velocity profiler (ACVP) [66], a combination of the multi-bistatic Acoustic Doppler Velocity Profiler (ADVP) technology with the multi-frequency Acoustic Backscattering System (ABS) technology, was used to measure time-resolved profiles of velocity and sediment concentration. For each flow condition, ensemble averaging over 11 similar experiment realizations is done to evaluate the mean profiles of velocity and sediment concentration. The high temporal resolution of the ACVP device allows for measuring the fluctuating component of velocity and sediment concentration which were used to estimate Reynolds shear stress and turbulent sediment flux. The two latter quantities were then used to estimate the turbulent Schmidt number. The Schmidt number was found to be constant with mean value = 0.44 while the von Karman "constant" was found to be = 0.225.

The numerical setup consists of a 1D mesh with vertical resolution $\Delta z = 0.4$ mm and time resolution $\Delta t = 10^{-4}$ s. The solution of the water mass conservation equation was kept off as in the previous cases with the same numerical scheme for the solution of the particle mass conservation equation. The flow was driven by a fixed mean pressure gra-

dient in the x-direction = 18.639 kg/m^2.s^2. The rheological parameters used in this case setup are shown in Table 4.

α_{max}	α_{min}^{fric}	C_p	C_1	C_2	B_ϕ	λ_r	μ_s	μ_2	I_o
0.58	0.53	0.05	3.0	5.0	0.66	10^{-6}	0.52	0.96	0.6

Table 4: The rheological parameters for turbulent sheet flow test case

The two-phase mixing length turbulence model [Eq. (50) and (51)] was initially used in this case with turbulent Schmidt number and von Karman constant equal 0.44 and 0.225, respectively, as obtained in the experiment. Chauchat [27] found that the value of mixing length model exponent e = 1.66 gives the best fit with the experimental data of Revil-Baudard et al. [105]. In the current study, this value was also found to give the best fit and thus has been used in the current test case. However, caution must be taken when using different rheological coefficients from those used by Chauchat [27] (shown in Table 4), this accordingly requires recalibration of this parameter.

The comparison between the experimental data and the numerical model results are shown in Figure 5 in terms of profiles of the velocity and the sediment concentration in both linear and logarithmic scales. This comparison shows good agreement between the experimental and numerical velocity profiles after calibration of the turbulence model. The deviation in the velocity profile in the near bed layer is thought to be mainly due to the inability of the simple mixing length closure to model the particle sediment interaction in the highly concentrated transition zone. Chauchat et al. [29] also figured out this shortcoming in the mixing length model and proposed using a 3D turbulence-resolving approach (i.e. LES) to capture this process. Note, however, that such a turbulence modelling approach is not evident, since it should take into account the finite size of the particles. The deviation of the velocity profile in the dilute layer may be due to overestimation of the eddy viscosity in this region. This conclusion is also confirmed by the overestimation of Reynolds stress.

In terms of the sediment concentration, the numerical results are in good agreement with the experimental data, and the small deviation may be attributed to the deviation in the velocity profile and consequently deviation of the velocity gradient.

Figure 6 shows a comparison between the experimental and numerical shear stress profiles (left) and between the numerical particle pressure and theoretical value of the immersed sediment weight. The Reynolds stress profile shows an overall agreement with the experimental data. However, the deviation, in this case, is more pronounced compared to the velocity and sediment concentration. This deviation is thought to be mainly due to overestimation of the eddy viscosity by the mixing length model. In addition to the shortcoming of the turbulence model, this deviation may be attributed to measurement errors.

The granular shear stress was not measured in the experiment. However, the overall behavior of granular shear stress profile is very similar to the results obtained by Chauchat et al. [29] using sedFoam 2.0. Finally, the comparison between numerical and theoretical particle pressure shows very good agreement as soon as the particle volume fraction reaches the α_{min}^{fric}.

ACCEPTED MANUSCRIPT

The same test case was repeated using an identical setup while using the mixture k-ε model described in §3.4 instead of the mixing length model. The parameter $\boldsymbol{B}$ in the drag-induced damping term [eq. (56)] was taken = 0.25 following Chauchat et al. [29], while the value of the parameter C_g in the buoyancy-induced damping term [eq. (54)] was taken = 1.0.

Figure 5 shows the improvement in the velocity profile in the near bed layer when using the mixture k -ε model compared to the mixing length model which implies that the modified k-ε model is more capable to model the particle-turbulence interaction in this layer. However the deviation of the velocity profile in the dilute layer still persists (or even increases). Again this indicates the overestimation of the eddy viscosity in this layer.

The sediment concentration profile is as good as the calibrated mixing length model as shown in Figure 5. The fluid shear stress and granular shear stress profiles were also improved when using the mixture k-ε model especially in the near bed highly concentrated layer as shown Figure 6.

The particle pressure gradient is also in good agreement with the theoretical value. However the model underestimates the magnitude of the particle pressure in this case. This is due to the fact that the value of the eddy viscosity in the stationary bed was not strictly = 0.0 which leads to a small value of the turbulent dispersion component of the slip velocity in this layer. This problem appears only in the 1D cases due to the use of cyclic boundary conditions at the inlet and outlet of the domain which causes gradual buildup of an unphysical eddy viscosity in the bed.

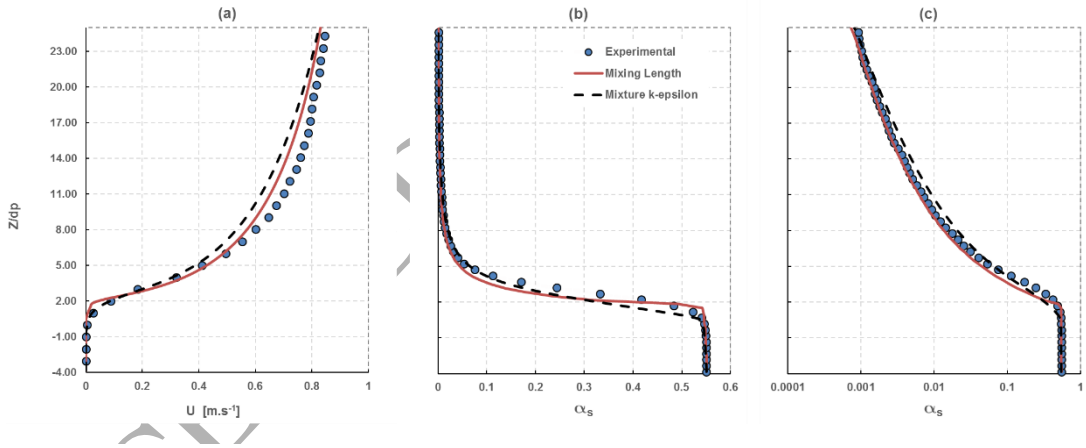


Figure 5: Comparison between the current numerical model and the experimental data of Revil-Baudard et al. [105] in terms of (a) streamwise velocity, (b) sediment concentration on linear scale, and (c) sediment concentration on log scale.

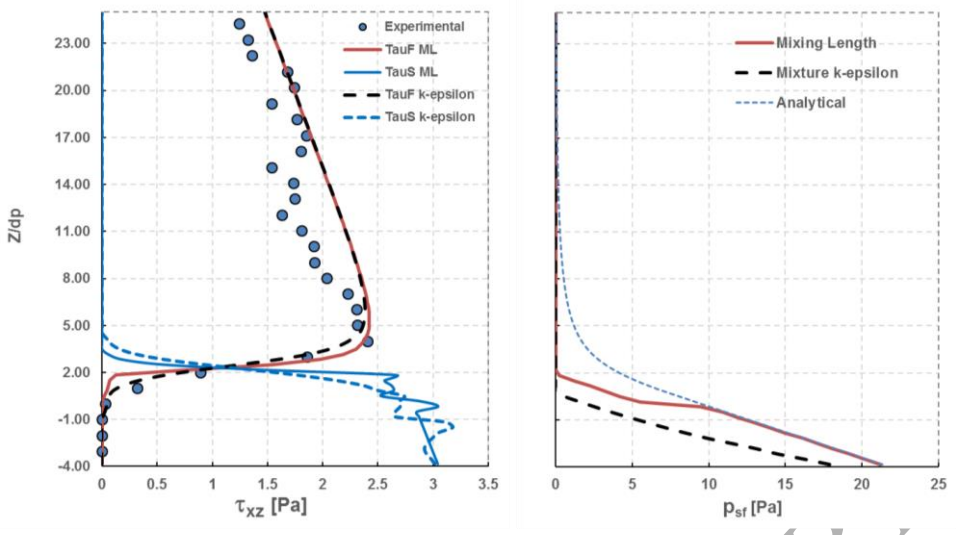


Figure 6: Comparison between current numerical model and the experimental data of Revil-Baudard et al. [105] in terms of fluid Reynolds stress and granular shear stress (left) and the numerical and analytical profile of particle pressure (right).

5.4 Scour due to a submerged horizontal jet

Hydraulic structures constructed along rivers or in coastal shallow waters, e.g. sluice gates, dam spillways or bridge piers change the local flow conditions which in turn can cause local scour around those structures. If the scour is significant and no protection measures were taken, this may eventually lead to undermining of those structures.

In this test case, the problem of local scour in front of a sluice gate due to a submerged horizontal jet is addressed in order to illustrate the capability of the current numerical model to simulate multi-dimensional problems in the presence of a free surface. The experimental data and setup from Chatterjee et al. [25] will be used for validation. The setup for this experiment is depicted in Figure 7.

In the current study run #2 from Chatterjee et al. [25] is chosen. In this test case, the gate opening $B_o = 2$ cm, apron length $L_A = 0.66$ m and sediment reservoir length $L_S = 2.10$ m. The water depth in front of the gate was initially fixed to 0.24 m using a control weir. A water head (Δh) of 0.118 m generates a submerged jet with entrance velocity $U_o = 1.02$ m/s. The particles are quartz sand with diameter $d_p = 0.76$ mm and density $\rho_s = 2650$ kg/m^3. The carrier fluid is water of density $\rho_f = 1000$ kg/m^3 and viscosity $\nu_f = 10^{-6}$ m^2/s.

To model this case, a 2DV mesh was prepared with uniform mesh size in all directions. Two mesh resolutions were tested in the current study: a coarse mesh with $\Delta x = \Delta z = 5$mm, and a fine mesh with $\Delta x = \Delta z = 2$ mm. The time step was variable during the simulation but constrained by a maximum $\Delta t = 10^{-4}$ s, and a maximum Courant number = 1.0. The upstream reservoir was removed from the solution domain to reduce the computational cost. The gate, apron and the bottom of the sediment reservoir were represented as wall boundary condition (fixed velocity = 0 m/s and zero gradient pressure). The velocity under the gate was explicitly defined with a fixed value = 1.02m/s in the x-direction and 0 in all other directions. For the water outlet and upper boundary, the total pressure was set to zero with zero gradient for velocity. The rheological and other physical parameters used in this case are shown in Table 5.

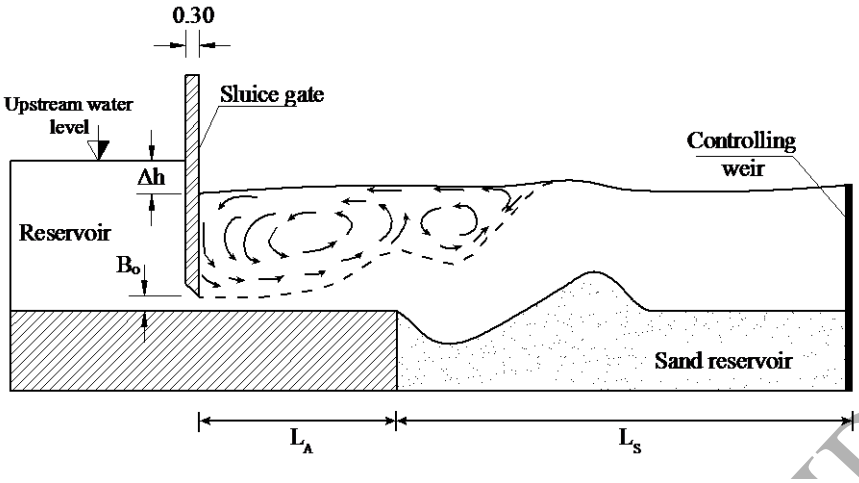


Figure 7: Sketch of the experimental setup for the submerged jet scour (adapted from Fig. 1 in [25])

Table 5: Rheological and physical parameters for submerged jet scour case

Sct	α_{max}	C_p	C_1	C_2	B_ϕ	λ_r	μ_s	μ_2	I_o
0.70	0.62	0.05	3.0	5.0	0.33	10^{-7}	0.55	0.9	0.6

For turbulence modeling, the mixture k-ε model was used in this case with the default model parameters shown in Table 1. For wall boundaries, smooth wall functions provided by OpenFOAM were used to provide the boundary conditions for k, ϵ and ν_t. For all other boundaries, a zero gradient boundary condition was imposed.

Figure 8 shows the time evolution of the bed scour profile and dune development during several moments in time for the fine mesh arrangement. Those snapshots show, qualitatively, that the model can reproduce the expected scour profile as observed in the experiment.

Moreover, Figure 9 shows, quantitatively, a comparison between scour profiles from Chatterjee et al. [25]and the current numerical model for both fine and coarse meshes. The newly developed model shows good agreement with the experiment in terms of magnitude and location of maximum scour depth, dune height and the front slope. The finer mesh results are slightly better especially in terms of predicting the maximum scour depth and the curvature of the dune crest. As expected, increasing the mesh resolution around the packed bed interface allows for better capturing the near bed physics and hence improving the model performance. However, due to the motion of this interface as a result of scour and sedimentation, this refinement should be done dynamically in order to reduce the computational cost.

The most obvious discrepancy between the numerical model and the experimental data is in terms of the rear slope of the dune. After one minute OpenFOAM underestimates the rear slope, while after three minutes, OpenFOAM overestimates that slope by using either coarse or fine meshes. This behavior may be due to the avalanching process that has been observed in both experiment and numerical simulation. This process causes a sudden decrease of the bed slope and this discrepancy seems to be due to a different timing of the corresponding avalanching events.

The avalanching process and hence the value of the rear slope may be sensitive to the choice of the rheological parameters, especially the static friction coefficient μ_s . In the current study we tested a range of μ_s values from 0.4 to 0.80. However, no significant change was observed between different cases.

In general, the numerical model was able to reproduce the experimental scour profile in this complicated case. Indeed the comprehensive model performance evaluation depends on the application and aimed accuracy.

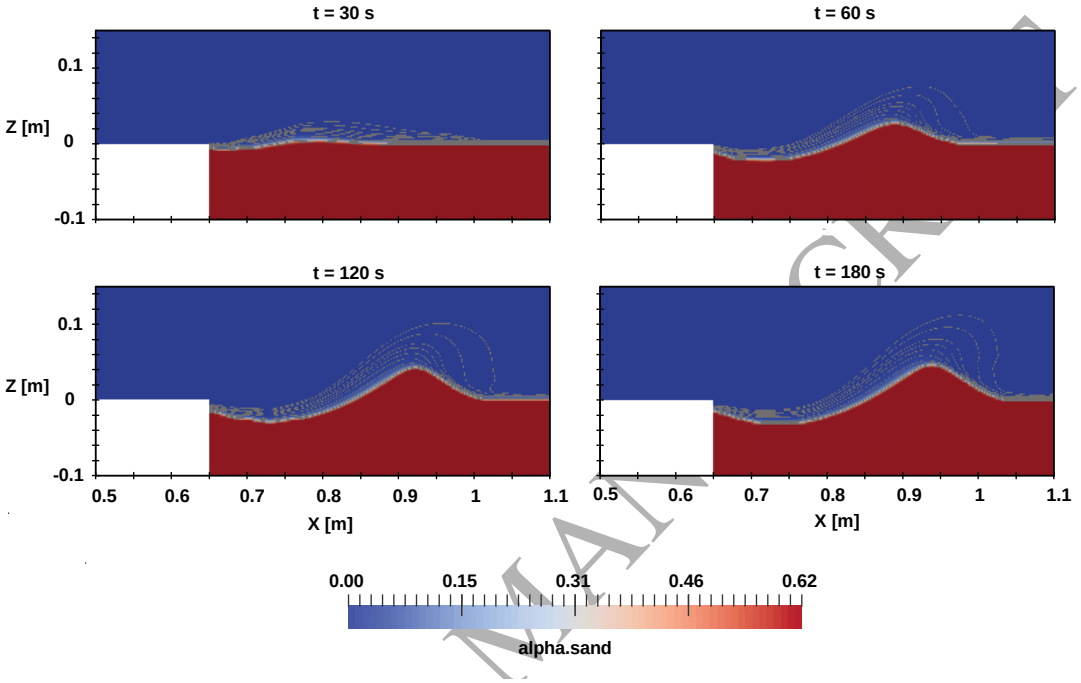


Figure 8: Evolution of the scour profile and dune at several time for the fine mesh arrangement. The shown contours represent sediment concentration.

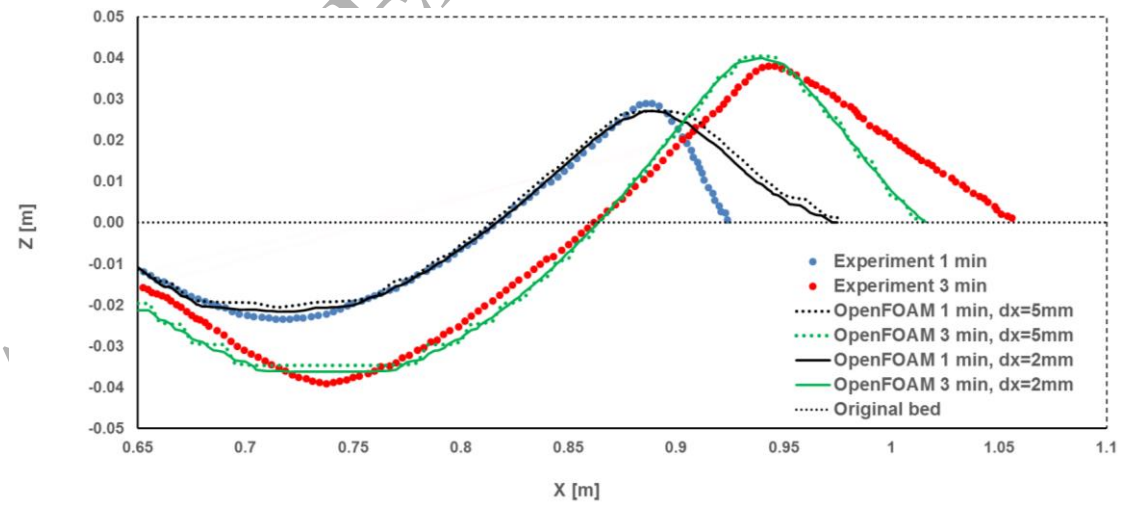


Figure 9: Comparison between scour profiles from Chatterjee et al. [25] and the current numerical model

5.5 Wave-induced scour under a submarine pipeline

ACCEPTED MANUSCRIPT

Submarine pipelines are used mainly to convey oil, gas or water at low cost. They are subjected to a combined action of waves and currents. When a pipeline is placed in a shallow water environment, it causes alternation of the local flow conditions, which eventually lead to the development of local scour around the pipeline. In addition to wave and current forces, scour is one of the main design criteria of submarine pipelines since it forms a free-spanning zone, in which the stresses in the pipeline are significantly increased.

The problem of pipeline scour in the marine environment was extensively studied over the past few decades. Most of this research effort was experimental work, e.g. Mao [95], Sumer et al. [115], Sumer and Fredsøe [113, 114], Cheng et al. [33]. Those experimental studies identify the main aspects which control the pipeline scour process e.g. the effect of the lee-wake, the Keulegan-Carpenter number (KC – see below), the Shields number (shear stress nondimensionalized by density, gravitational acceleration and particle diameter) and the gap between pipeline and the seabed.

In this last test case the local scour under a submarine pipeline due to wave action only is addressed. The main objective here is to evaluate the current model's capability to account for the interaction between the free surface dynamics, exemplified here by wave motion, and sediment dynamics. To quantitatively evaluate the model performance, the model results are compared with experimental measurements. The experimental data and setup from Sumer and Fredsøe [113] are used for validation. In the current study, test number (3) was selected for this purpose.

The experiment was carried out in a piston type wave flume of width equal 0.6 m and mean water depth fixed at h = 0.40 m. A hydraulically smooth pipe of diameter D = 0.05 m was placed in contact with a packed sand bed. The sand used in this experiment has a median particle diameter d_{50} = 0.58 mm and density = 2700 kg/m^3. The carrier fluid is water of density ρ_f = 1000 kg/m^3 and viscosity $\nu_f = 10^{-6}$ m^2/s.

According to Sumer and Fredsøe [113], the Keulegan-Carpenter number (KC) is the key parameter that determines the waves-induced equilibrium scour depth under a pipeline. KC is given by:

$$KC = \frac{U_m T_w}{D} = 2\pi \frac{a}{D}, \tag{63}$$

where U_m is maximum flow velocity just outside the wave boundary layer , T_w is the wave period and a is amplitude of the maximum horizontal particle excursion. In the selected test, KC = 7.0 was achieved with wave of T_w = 1.43 s. and U_m = 0.228 m/s.

The 2DV numerical domain and mesh used in the current case is shown in Figure 10. The initial sediment bed thickness is 2xD = 0.1 m and the free surface is 0.40 meter above the bed. The pipeline is placed in the center of the domain and the domain extends 70xD in each direction. The mesh has variable size ranging from 5 mm at the free surface to 1 mm at the bed interface. Additional mesh refinement was applied in the vicinity of the pipeline in order to enable capturing of the boundary layer and the lee-wake of the pipe. The time step was variable during the simulation but constrained by a maximum $\Delta t = 10^{-4}$ s, and a maximum Courant number = 1.0.

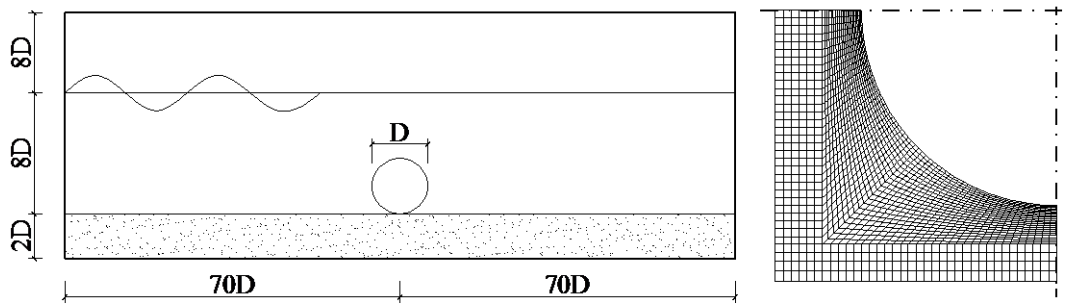


Figure 10: The computational domain (left) and the mesh in vicinity of the pipeline (right) used in the pipeline scour test case.

In order to provide the wave generation boundary condition at the inlet and the wave absorption boundary condition at the outlet, the current numerical model was coupled with the olaFlow wave generation/absorption library [59]. The wave generation boundary condition allows for wave generation at the inlet by specifying the horizontal velocity, vertical velocity, and the water level (i.e. water phase fraction) that correspond to a user-selected wave theory. It also provides an active wave absorption boundary condition at the outlet that allows the wave leaving the domain with minimum reflection.

In the current study, Stokes 2nd order wave theory was selected for wave generation at the inlet which is applicable for the experimental wave conditions according to the Le Méhauté diagram for the limits of validity for various wave theories [88]. Although the wave height was not explicitly reported in Sumer and Fredsøe [113], the wave height H_w = 0.15 m was found to correspond to U_m = 0.228 m/s for waves of period T_w = 1.43 s. in water depth h = 0.4 m according to Stokes 2nd order wave theory. For the upper boundary, the total pressure was set to zero with zero gradient for velocity. For the lower boundary and the pipeline, a fixed velocity = 0 m/s and a zero gradient for pressure was set.

According to Sumer and Fredsøe [113] the lee-wake of the pipe is the main action that governs the scour below a pipeline in waves. In order to model this process adequately, the mixture k-ε model described in §3.4 was used for turbulence modeling in this case. However, it is well known that the RANS-based turbulence models (e.g. k-ε model) severely overestimate the turbulence kinetic energy and eddy viscosity in surface waves due to large strain rates at the free surface [42, 85, 100]. This overestimation of eddy viscosity leads to unphysical wave damping. Moreover, in the current case, this leads to unphysical surface deformation when partial breaking of waves takes place.

The current model already contains a buoyancy damping term [Eq. (54)] which is also active at the water-air interface due to density gradient at this region. However, this term alone was not enough to avoid overestimation of turbulence levels especially if partial wave breaking take place. To tackle this problem, an additional turbulence damping term at the free surface was added to Eq. (53) and Eq. (60). This term was suggested by Naot and Rodi [100] and given by:

$$D_{fs} = -\frac{c_\mu^{-\frac{1}{4}}}{\kappa} k^{\frac{1}{2}} y', \tag{64}$$

ACCEPTED MANUSCRIPT

where $\kappa = 0.40$ is the von Karman constant and $y' = 0.07$h is the virtual origin of the turbulent length scale [61]. This term is applied only at the free surface using a Dirac delta function, defined as:

$$\delta(\gamma) = \begin{cases} 1.0 & \|\nabla\gamma\| > 0 \\ 0 & \|\nabla\gamma\| = 0 \end{cases} \tag{65}$$

Adding this term to the mixture k-ε model equations yields a stable solution without any noticable damping or unphysical deformation of the free surface. For turbulence model boundary conditions, smooth wall functions were used to provide the boundary conditions for k, ε and ν_t at the pipe surface. For all other boundaries, zero gradient boundary condition was imposed. The rheological and other physical parameters used in this case are the same as used in the jet scour test case which are shown in Table 5.

Figure 11 illustrates the interaction between the surface wave dynamics, the pipeline and the sediment bed. The zoomed view in Figure 11 (middle panel) shows the ability of the current numerical model to capture the role of vortex shedding in the scour process. Moreover, the presence of the pipeline caused increase of the near-bed wave-induced velocities in the gap between the bed and the pipeline. This gives rise to the so-called "tunnel erosion" below the pipeline which is one of the curcial aspects that controls the pipeline scour especially in the initial stages [86].

In the lower panels of Figure 11, the temporal evolution of the bed scour profile is depicted at time t = 12, 180 and 300 seconds from the start of the simulation. Those snapshots show a qualitative similarity to the scour profiles reported in Sumer and and Fredsøe [113].

A more qualitative comparison between the current numerical model and the experimental results of Sumer and and Fredsøe [113] is shown in Figure 12 for $KC = 7.0$. At t = 12 s. the modeled relative scour depth is $d_s/D = 0.20$ matches very well with the corresponding experimental value of 0.19. The streamwise extension of the scour hole is in range $-1.2 < B_s/D < 1.20$ which slightly overestimates the experimental values especially in the upstream side of the pipeline. In the lower panel of Figure 12 the comparison at 300 s. is shown. The modeled relative scour depth is $d_s/D = 0.25$ in this case which is the same as observed in the experiment at the same time instance. The streamwise extension of the scour hole also in a good agreement with the experimental values. However, at this time instance, the upstream and the downstream sand dunes were washed out completely by the vortex shedding in the numerical model which is not the case in the experiment. This is thought to be mainly due to the overestimation of the eddy viscosity in the wake of the pipeline by the k-ε model, which is known to overestimate the turbulent kinetic energy and the eddy viscosity in the separated flow [80].

In general, this test case illustrates the capability of the current numerical model as a framework to model the interaction between turbulent free surface flow and sediment transport allowing to investigate the underlying processes that drive this interaction.

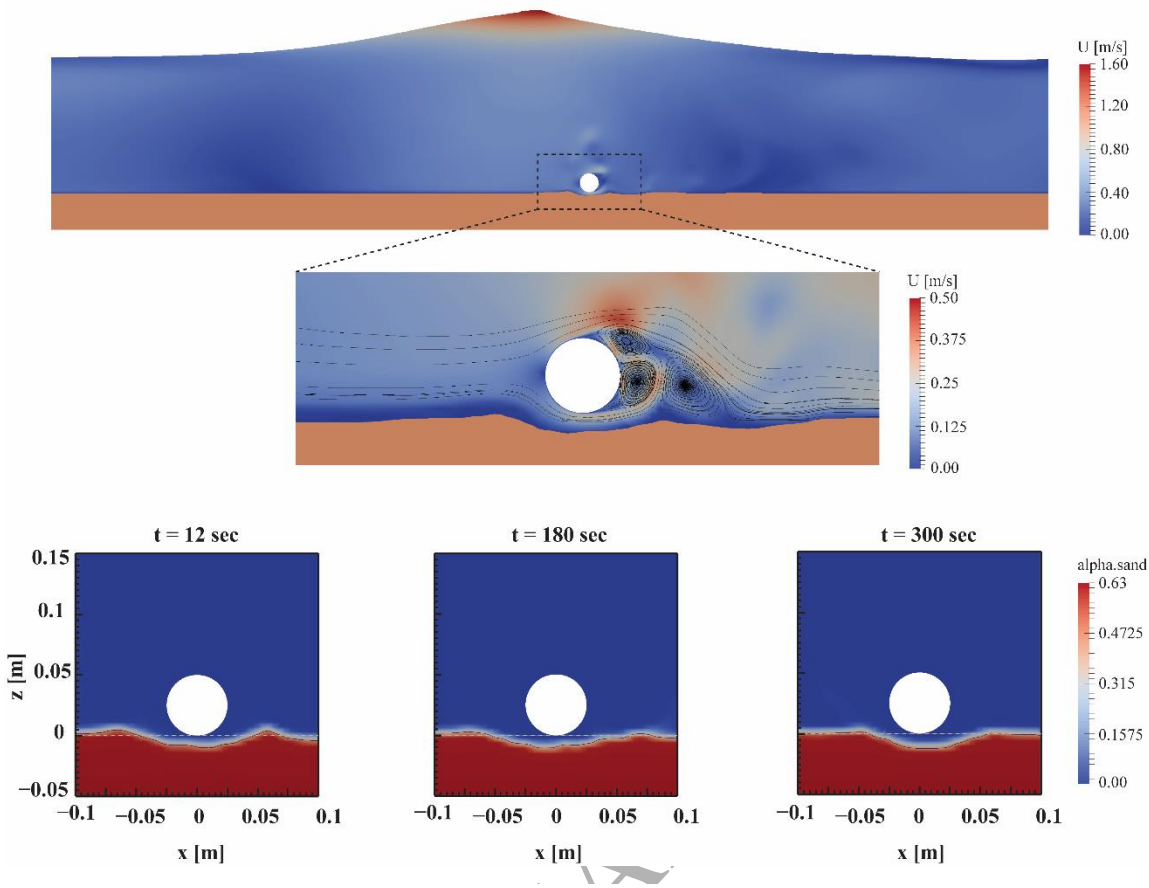


Figure 11: A wave crest passing over a submarine pipeline (upper panel), causing vortex shedding in the wake of it (middle panel), and the time evolution of the scour profile below the pipeline at several time instances (lower panels).

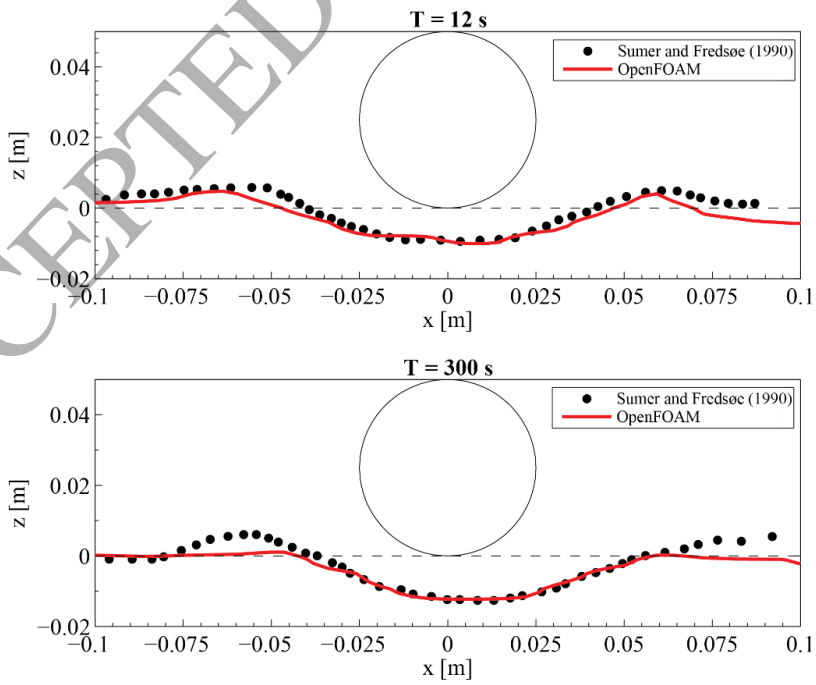


Figure 12: Comparison of the sour profile from Sumer and Fredsøe [113] test No. 3 and the current numerical model after 12 seconds (upper panel) and 300 seconds (lower panel).

ACCEPTED MANUSCRIPT

6. Conclusions & Perspectives

In the current study, the development of a new physics-based model for sediment transport in free surface flows and its numerical implementation within OpenFOAM framework were introduced. The core model equations were derived based on the fundamental multiphase mixture theory including a modified VOF equation for free surface tracking in sediment-laden flow. The new model exploits the recently developed dense granular flow rheology to provide the required closures for sediment stresses. In addition, different options for mixture viscosity and drag coefficient are provided and can be selected in the runtime. Two-phase mixing length or mixture k-ε turbulence models were used to model the turbulent stress tensor. In the mixture k-ε model the effect of buoyancy and drag on turbulence damping were included. In free surface flows undergoing high deformations, e.g. wave breaking, an optional damping term was applied at the free surface to avoid excessive turbulence generation.

The model has been validated using five different test cases to investigate the model capabilities and features in different sediment flow conditions. The first test case of pure sedimentation of non-cohesive particles allows for testing the ability of the model to predict the correct hindered settling velocity and to calibrate the drag model. The second test case involves laminar bedload transport was used to validate the numerical implementation of the granular rheology closures.

The third test case of turbulent sheet flow in unidirectional flow illustrates the capability of the model to simulate dense sediment transport taking into account the particle-particle interaction which plays an important role in this regime. This case shows that the model is sensitive to the results of the turbulence closure which must be chosen and calibrated carefully in order to obtain accurate results.

The fourth test case of jet scour illustrate the capability of the model to simulate multi-dimensional complex sediment transport problems in the presence of the free surface. The corresponding model results are in good agreement with the experimental results and the potential reasons for the remaining discrepancies can be identified.

The last test case focusses mainly on the interaction between free surface dynamics and the dynamics of sediment. In this case the wave-induced scour under a submarine pipeline was investigated. The numerical model was able to capture the key processes that governs the scouring process, including the vortex shedding in the wake of the pipeline and the tunnel erosion. Hence, the model results are in a good agreement with the experimental observations.

As a general conclusion, the new model was able to reproduce the experimental data in different flow conditions with a reasonable agreement. Additional validation and test cases will be addressed in future studies in order to obtain a comprehensive model performance evaluation. The new model is still under active development. Improving the turbulence closures and adding the capability of dynamic mesh refinement on the interface are of main interest. A unified granular rheology closure that allows for smooth transition from the viscous to the inertial regime is under development and testing in order to replace the currently used regime-based closures.

For sure, there remain many features and process closures of the model which can be and are expected to be improved in the future. For instance, it will be meaningful to consider the development of another closure for the dynamic pressure expressed in terms of the turbulent kinetic energy, which is available anyhow from the turbulence model,

ACCEPTED MANUSCRIPT

since it can be related to the granular temperature. Also the turbulent Schmidt number, relating eddy diffusivity to eddy viscosity [119, 120], requires a better and more general closure which remains valid in non-dilute conditions. Different methods can contribute, here, including further advancements in kinetic theory and granular fluidity models. The recently developed models based on the Material Point Method (a particle-in-cell method), originally developed for silo flow problems [128] may also provide an interesting alternative tool. Applications of this method include the simulation of landslide problems [24] and fluidization of soils [16].

Acknowledgements

This research was supported by a PhD scholarship for the 1st author provided by KU Leuven's Interfaculty Council for Development Cooperation (IRO Scholarship) to which the authors are most grateful. We would also like to show our gratitude to Alexandria University for allowing long leave of absence for the 1st author in order to obtain his PhD. The acknowledgement also extends to the developers of OpenFOAM which was used as a base for current numerical model development.

ACCEPTED MANUSCRIPT

ACCEPTED MANUSCRIPT

References

1. Amoudry, L., *A review on coastal sediment transport modelling.* Proudman Oceanographic Laboratory, 2008. **Internal Report No. 189**.
2. Amoudry, L., T.J. Hsu, and P.F. Liu, *Two-phase model for sand transport in sheet flow regime.* Journal of Geophysical Research: Oceans, 2008. **113**(C3).
3. Amoudry, L.O. and A.J. Souza, *Deterministic coastal morphological and sediment transport modeling: A review and discussion.* Reviews of Geophysics, 2011. **49**(2).
4. Andersson, K.B., *Pressure drop in ideal fluidization.* Chemical Engineering Science, 1961. **15**(3-4): p. 276-297.
5. Aussillous, P., J. Chauchat, M. Pailha, M. Médale, and E. Guazzelli, *Investigation of the mobile granular layer in bedload transport by laminar shearing flows.* Journal of Fluid Mechanics, 2013. **736**: p. 594-615.
6. Azuma, R. and I. Nezu. *Velocity profiles and von Karman constant in open-channel flows with suspended sediment*. 4th Int. Symp. on Environmental Hydraulics. Vol. 2004.
7. Bagnold, R.A., *Experiments on a gravity-free dispersion of large solid spheres in a Newtonian fluid under shear.* Proceedings of the Royal Society of London. Series A. Mathematical and Physical Sciences, 1954. **225**(1160): p. 49-63.
8. Batchelor, G. and J. Green, *The determination of the bulk stress in a suspension of spherical particles to order c 2.* Journal of Fluid Mechanics, 1972. **56**(3): p. 401-427.
9. Bercovier, M. and M. Engelman, *A finite-element method for incompressible non-Newtonian flows.* Journal of Computational Physics, 1980. **36**(3): p. 313-326.
10. Berzi, D. and L. Fraccarollo, *Intense sediment transport: Collisional to turbulent suspension.* Physics of Fluids, 2016. **28**(2): p. 023302.
11. Berzi, D. and J.T. Jenkins, *Steady shearing flows of deformable, inelastic spheres.* Soft matter, 2015. **11**(24): p. 4799-4808.
12. Berzi, D. and D. Vescovi, *Different singularities in the functions of extended kinetic theory at the origin of the yield stress in granular flows.* Physics of fluids, 2015. **27**(1): p. 013302.
13. Best, J., S. Bennett, J. Bridge, and M. Leeder, *Turbulence modulation and particle velocities over flat sand beds at low transport rates.* Journal of Hydraulic Engineering, 1997. **123**(12): p. 1118-1129.
14. Bird, R.B., W.E. Stewart, and E.N. Lightfoot, *Transport phenomena*. 2007: John Wiley & Sons.
15. Bohorquez, P., *Study and numerical simulation of sediment transport in free-surface flow*. 2008, University of Malaga, Spain.
16. Bolognin, M., M. Martinelli, K.J. Bakker, and S.N. Jonkman, *Validation of material point method for soil fluidisation analysis.* Journal of Hydrodynamics, Ser. B, 2017. **29**(3): p. 431-437.
17. Boyer, F., É. Guazzelli, and O. Pouliquen, *Unifying suspension and granular rheology.* Physical Review Letters, 2011. **107**(18): p. 188301.
18. Brackbill, J., D.B. Kothe, and C. Zemach, *A continuum method for modeling surface tension.* Journal of computational physics, 1992. **100**(2): p. 335-354.
19. Breedveld, L.V.A., *Shear-induced self-diffusion in concentrated suspensions.* 2000.
20. Brouwers, H., *Particle-size distribution and packing fraction of geometric random packings.* Physical review E, 2006. **74**(3): p. 031309.
21. Cao, Z., S. Egashira, and P.A. Carling, *Role of suspended-sediment particle size in modifying velocity profiles in open channel flows.* Water resources research, 2003. **39**(2).
22. Cao, Z., L. Wei, and J. Xie, *Sediment-laden flow in open channels from two-phase flow viewpoint.* Journal of hydraulic engineering, 1995. **121**(10): p. 725-735.

ACCEPTED MANUSCRIPT

ACCEPTED MANUSCRIPT

23. Cassar, C., M. Nicolas, and O. Pouliquen, *Submarine granular flows down inclined planes.* Physics of fluids, 2005. **17**(10): p. 103301.
24. Ceccato, F., I. Redaelli, C. di Prisco, and P. Simonini, *Impact forces of granular flows on rigid structures: Comparison between discontinuous (DEM) and continuous (MPM) numerical approaches.* Computers and Geotechnics, 2018. **103**: p. 201-217.
25. Chatterjee, S., S. Ghosh, and M. Chatterjee, *Local scour due to submerged horizontal jet.* Journal of Hydraulic Engineering, 1994. **120**(8): p. 973-992.
26. Chauchat, J., *Contribution to two-phase flow modeling for sediment transport in estuarine and coastal zones*. 2007, PhD Thesis, University of Caen, France (in French).
27. Chauchat, J., *A comprehensive two-phase flow model for unidirectional sheet-flows.* Journal of Hydraulic Research, 2018. **56**(1): p. 15-28.
28. Chauchat, J., Z. Cheng, CyrilleBonamy, T. Nagel, and T.-J. Hsu: Sedfoam/Sedfoam: Release 2.0, https://doi.org/10.5281/zenodo.836643, 2017.
29. Chauchat, J., Z. Cheng, T. Nagel, C. Bonamy, and T.-J. Hsu, *SedFoam-2.0: a 3-D two-phase flow numerical model for sediment transport.* Geoscientific Model Development, 2017. **10**(12): p. 4367.
30. Chauchat, J. and S. Guillou, *On turbulence closures for two-phase sediment-laden flow models.* Journal of Geophysical Research: Oceans, 2008. **113**(C11).
31. Chauchat, J. and M. Médale, *A three-dimensional numerical model for dense granular flows based on the μ (I) rheology.* Journal of Computational Physics, 2014. **256**: p. 696-712.
32. Cheng, D., *Viscosity-concentration equations and flow curves for suspensions.* CHEMISTRY & INDUSTRY, 1980(10): p. 403-406.
33. Cheng, L., K. Yeow, Z. Zang, and F. Li, *3D scour below pipelines under waves and combined waves and currents.* Coastal engineering, 2014. **83**: p. 137-149.
34. Cheng, N.-S., *Analysis of velocity lag in sediment-laden open channel flows.* Journal of hydraulic engineering, 2004. **130**(7): p. 657-666.
35. Cheng, Z., *A multi-dimensional two-phase flow modeling framework for sediment transport applications*. 2016, UNIVERSITY OF DELAWARE.
36. Cheng, Z., T.-J. Hsu, and J. Chauchat, *An Eulerian two-phase model for steady sheet flow using large-eddy simulation methodology.* Advances in Water Resources, 2018. **111**: p. 205-223.
37. Chialvo, S., J. Sun, and S. Sundaresan, *Bridging the rheology of granular flows in three regimes.* Physical review E, 2012. **85**(2): p. 021305.
38. Cooper, A. and M. Dearnaley, *Guidelines for the use of computational models in coastal and estuarial studies-flow and sediment transport models.* 1996.
39. Damián, S.M., *An extended mixture model for the simultaneous treatment of short and long scale interfaces.* Dissertationsschrift, Universidad Nacional del Litoral, Argentinien. Krepper, E., Lucas, D., Frank, T., Prasser, H.-M., & Zwart, PJ (2008). The inhomogeneous MUSIG model for the simulation of polydispersed flows. Nuclear Engineering and Design, 2013. **238**(7): p. 1690-1702.
40. Dean, R.G. and R.A. Dalrymple, *Water wave mechanics for engineers and scientists*. Vol. 2. 1991: world scientific publishing Co Inc.
41. Deutsch, E. and O. Simonin. *Large eddy simulation applied to the motion of particles in stationary homogeneous fluid turbulence*. Proc. of ASME-FED. Vol. 110: 35-42, 1991. New York.
42. Devolder, B., P. Rauwoens, and P. Troch, *Application of a buoyancy-modified k-ω SST turbulence model to simulate wave run-up around a monopile subjected to regular waves using OpenFOAM®.* Coastal Engineering, 2017. **125**: p. 81-94.

ACCEPTED MANUSCRIPT

43. Drake, T.G. and J. Calantoni, *Discrete particle model for sheet flow sediment transport in the nearshore.* Journal of Geophysical Research: Oceans, 2001. **106**(C9): p. 19859-19868.
44. Drew, D., *Turbulent sediment transport over a flat bottom using momentum balance.* Journal of Applied Mechanics, 1975. **42**(1): p. 38-44.
45. Drew, D.A. and S.L. Passman, *Theory of multicomponent fluids*. Vol. 135. 2006: Springer Science & Business Media.
46. Eckstein, E.C., D.G. Bailey, and A.H. Shapiro, *Self-diffusion of particles in shear flow of a suspension.* Journal of Fluid Mechanics, 1977. **79**(1): p. 191-208.
47. Einstein, A., *Berichtigung zu meiner Arbeit:„Eine neue Bestimmung der Moleküldimensionen"* . Annalen der Physik, 1911. **339**(3): p. 591-592.
48. Einstein, H.A., *Effect of heavy sediment concentration near the bed on velocity and sediment distribution.* University of California, Berkeley, Calif., 1955. **33**: p. 2.
49. Elghobashi, S., *On predicting particle-laden turbulent flows.* Applied Scientific Research, 1994. **52**(4): p. 309-329.
50. Elghobashi, S. and T. Abou-Arab, *A two-equation turbulence model for two-phase flows.* The Physics of Fluids, 1983. **26**(4): p. 931-938.
51. Favre, A., *Equations des gaz turbulents compressibles.* J. de Mécanique, 1965. **4**(3).
52. Finn, J.R., M. Li, and S.V. Apte, *Particle based modelling and simulation of natural sand dynamics in the wave bottom boundary layer.* Journal of Fluid Mechanics, 2016. **796**: p. 340-385.
53. Forterre, Y. and O. Pouliquen, *Flows of dense granular media.* Annu. Rev. Fluid Mech., 2008. **40**: p. 1-24.
54. Frigaard, I. and C. Nouar, *On the usage of viscosity regularisation methods for visco-plastic fluid flow computation.* Journal of non-newtonian fluid mechanics, 2005. **127**(1): p. 1-26.
55. Gadala-Maria, F.A., *The rheology of concentrated suspensions*. 1979: Dept. of Chemical Engineering.
56. Greimann, B., M. Muste, and F. Holly Jr, *Two-phase formulation of suspended sediment transport.* Journal of Hydraulic Research, 1999. **37**(4): p. 479-500.
57. Henkes, R., F. Van Der Vlugt, and C. Hoogendoorn, *Natural-convection flow in a square cavity calculated with low-Reynolds-number turbulence models.* International Journal of Heat and Mass Transfer, 1991. **34**(2): p. 377-388.
58. Herrmann, M.J. and O.S. Madsen, *Effect of stratification due to suspended sand on velocity and concentration distribution in unidirectional flows.* Journal of Geophysical Research: Oceans, 2007. **112**(C2).
59. Higuera, P.: phicau/olaFlow: CFD for waves, https://doi.org/10.5281/zenodo.1297013, 2018.
60. Hirt, C.W. and B.D. Nichols, *Volume of fluid (VOF) method for the dynamics of free boundaries.* Journal of computational physics, 1981. **39**(1): p. 201-225.
61. Hossain, M. and W. Rodi. *Mathematical modelling of vertical mixing in stratified channel flow*. Proc. 2nd Int. Symp. on Stratified Flows, Trondheim, Norway, 1980. Vol. 1980.
62. Houssais, M., C.P. Ortiz, D.J. Durian, and D.J. Jerolmack, *Rheology of sediment transported by a laminar flow.* Physical Review E, 2016. **94**(6): p. 062609.
63. Hsu, T.-J., J.T. Jenkins, and P.L.-F. Liu. *On two-phase sediment transport: sheet flow of massive particles*. Proceedings of the Royal Society of London A: Mathematical, Physical and Engineering Sciences. Vol. 460: 2223-2250, 2004. The Royal Society.
64. Hsu, T.J., J.T. Jenkins, and P.L.F. Liu, *On two-phase sediment transport: Dilute flow.* Journal of Geophysical Research: Oceans, 2003. **108**(C3).

ACCEPTED MANUSCRIPT

65. Hunt, J., *The turbulent transport of suspended sediment in open channels.* Proc. R. Soc. Lond. A, 1954. **224**(1158): p. 322-335.
66. Hurther, D., P.D. Thorne, M. Bricault, U. Lemmin, and J.-M. Barnoud, *A multi-frequency Acoustic Concentration and Velocity Profiler (ACVP) for boundary layer measurements of fine-scale flow and sediment transport processes.* Coastal Engineering, 2011. **58**(7): p. 594-605.
67. Ishii, M. and T. Hibiki, *Thermo-fluid dynamics of two-phase flow*. 2010: Springer Science & Business Media.
68. Jackson, R., *The dynamics of fluidized particles*. 2000: Cambridge University Press.
69. JAEGER, H.M. and S.R. NAGEL, *Physics of the Granular State.* Science, 1992. **255**(5051): p. 1523-1531.
70. Jasak, H., *Error analysis and estimation for finite volume method with applications to fluid flow.* 1996.
71. Jenkins, J.T., *Dense shearing flows of inelastic disks.* Physics of Fluids, 2006. **18**(10): p. 103307.
72. Jenkins, J.T., *Dense inclined flows of inelastic spheres.* Granular matter, 2007. **10**(1): p. 47-52.
73. Jenkins, J.T. and S.B. Savage, *A theory for the rapid flow of identical, smooth, nearly elastic, spherical particles.* Journal of fluid mechanics, 1983. **130**: p. 187-202.
74. Jha, S.K. and F.A. Bombardelli, *Toward two-phase flow modeling of nondilute sediment transport in open channels.* Journal of Geophysical Research: Earth Surface, 2010. **115**(F3).
75. Joel, H. and M.F. Peric, *Computational methods for fluid dynamics.* 1999.
76. Johnson, P.C. and R. Jackson, *Frictional–collisional constitutive relations for granular materials, with application to plane shearing.* Journal of fluid Mechanics, 1987. **176**: p. 67-93.
77. Johnson, P.C., P. Nott, and R. Jackson, *Frictional–collisional equations of motion for participate flows and their application to chutes.* Journal of fluid mechanics, 1990. **210**: p. 501-535.
78. Jop, P., Y. Forterre, and O. Pouliquen, *A constitutive law for dense granular flows.* Nature, 2006. **441**(7094): p. 727.
79. Kamrin, K. and G. Koval, *Nonlocal constitutive relation for steady granular flow.* Physical Review Letters, 2012. **108**(17): p. 178301.
80. Kato, M. and B.E. Launder, *The modelling of turbulent flow around stationary and vibrating square cylinders.* Turbulent Shear Flow, 1993. **1**: p. 10.4. 1-10.4. 6.
81. Kim, Y., Z. Cheng, T.J. Hsu, and J. Chauchat, *A Numerical Study of Sheet Flow Under Monochromatic Nonbreaking Waves Using a Free Surface Resolving Eulerian Two-Phase Flow Model.* Journal of Geophysical Research: Oceans, 2018. **123**(7): p. 4693-4719.
82. Kobayashi, N. and S.N. Seo, *Fluid and sediment interaction over a plane bed.* Journal of Hydraulic Engineering, 1985. **111**(6): p. 903-921.
83. Krieger, I.M. and T.J. Dougherty, *A mechanism for non-Newtonian flow in suspensions of rigid spheres.* Transactions of the Society of Rheology, 1959. **3**(1): p. 137-152.
84. Lalli, F., P.G. Esposito, R. Piscopia, and R. Verzicco, *Fluid–particle flow simulation by averaged continuous model.* Computers & fluids, 2005. **34**(9): p. 1040-1061.
85. Larsen, B.E. and D.R. Fuhrman, *On the over-production of turbulence beneath surface waves in Reynolds-averaged Navier–Stokes models.* Journal of Fluid Mechanics, 2018. **853**: p. 419-460.

ACCEPTED MANUSCRIPT

86. Larsen, B.E., D.R. Fuhrman, and B.M. Sumer, *Simulation of wave-plus-current scour beneath submarine pipelines.* Journal of Waterway, Port, Coastal, and Ocean Engineering, 2016. **142**(5): p. 04016003.
87. Launder, B.E. and D.B. Spalding, *Mathematical models of turbulence*. 1972: Academic press.
88. Le Méhauté, B., *An introduction to hydrodynamics and water waves*. 2013: Springer Science & Business Media.
89. Lee, C.-H., Y.M. Low, and Y.-M. Chiew, *Multi-dimensional rheology-based two-phase model for sediment transport and applications to sheet flow and pipeline scour.* Physics of Fluids, 2016. **28**(5): p. 053305.
90. Lee, C.-H., C. Xu, and Z. Huang, *A three-phase flow simulation of local scour caused by a submerged wall jet with a water-air interface.* Advances in Water Resources, 2017.
91. Leighton, D. and A. Acrivos, *Viscous resuspension.* Chemical Engineering Science, 1986. **41**(6): p. 1377-1384.
92. Li, L. and M. Sawamoto, *Multi-phase model on sediment transport in sheet-flow regime under oscillatory flow.* Coastal Engineering in Japan, 1995. **38**(2): p. 157-178.
93. Lun, C., S.B. Savage, D. Jeffrey, and N. Chepurniy, *Kinetic theories for granular flow: inelastic particles in Couette flow and slightly inelastic particles in a general flowfield.* Journal of fluid mechanics, 1984. **140**: p. 223-256.
94. Manninen, M., V. Taivassalo, and S. Kallio, *On the mixture model for multiphase flow*. 1996, Technical Research Centre of Finland Finland.
95. Mao, Y., *The interaction between a pipeline and an erodible bed.* Series Paper Technical University of Denmark, 1987(39).
96. Matoušek, V. and Š. Zrostlík, *Laboratory testing of granular kinetic theory for intense bed load transport.* Journal of Hydrology and Hydromechanics, 2018. **66**(3): p. 330-336.
97. MiDi, G., *On dense granular flows.* The European Physical Journal E, 2004. **14**(4): p. 341-365.
98. Mueller, S., E. Llewellin, and H. Mader. *The rheology of suspensions of solid particles*. Proceedings of the Royal Society of London A: Mathematical, Physical and Engineering Sciences. Vol. 466: 1201-1228, 2010. The Royal Society.
99. Muste, M. and V. Patel, *Velocity profiles for particles and liquid in open-channel flow with suspended sediment.* Journal of hydraulic engineering, 1997. **123**(9): p. 742-751.
100. Naot, D. and W. Rodi, *Calculation of secondary currents in channel flow.* Journal of the Hydraulics Division, 1982. **108**(8): p. 948-968.
101. Ouriemi, M., P. Aussillous, and E. Guazzelli, *Sediment dynamics. Part 1. Bed-load transport by laminar shearing flows.* Journal of Fluid Mechanics, 2009. **636**: p. 295-319.
102. Papanastasiou, T.C., *Flows of materials with yield.* Journal of Rheology, 1987. **31**(5): p. 385-404.
103. Papanicolaou, A.N., M. Elhakeem, G. Krallis, S. Prakash, and J. Edinger, *Sediment transport modeling review—current and future developments.* Journal of Hydraulic Engineering, 2008. **134**(1): p. 1-14.
104. Parker, G. and N.L. Coleman, *Simple model of sediment-laden flows.* Journal of Hydraulic Engineering, 1986. **112**(5): p. 356-375.
105. Revil-Baudard, T., J. Chauchat, D. Hurther, and P.-A. Barraud, *Investigation of sheet-flow processes based on novel acoustic high-resolution velocity and concentration measurements.* Journal of Fluid Mechanics, 2015. **767**: p. 1-30.

ACCEPTED MANUSCRIPT

ACCEPTED MANUSCRIPT

106. Revil-Baudard, T. and J. Chauchat, *A two-phase model for sheet flow regime based on dense granular flow rheology.* Journal of Geophysical Research: Oceans, 2013. **118**(2): p. 619-634.
107. Rodi, W., *Turbulence models and their applications in hydraulics-a state-of-the-art review.* IAHR monograph, 1984.
108. Roelvink, D., *A guide to modeling coastal morphology*. Vol. 12. 2011: world scientific.
109. Rouse, H., *Modern conceptions of the mechanics of fluid turbulence.* Trans ASCE, 1937. **102**: p. 463-505.
110. Rusche, H., *Computational fluid dynamics of dispersed two-phase flows at high phase fractions*. 2003, Imperial College London (University of London).
111. Savage, S. and D. Jeffrey, *The stress tensor in a granular flow at high shear rates.* Journal of Fluid Mechanics, 1981. **110**: p. 255-272.
112. Schmeeckle, M.W., *Numerical simulation of turbulence and sediment transport of medium sand.* Journal of Geophysical Research: Earth Surface, 2014. **119**(6): p. 1240-1262.
113. Sumer, B.M. and J. Fredsøe, *Scour below pipelines in waves.* Journal of waterway, port, coastal, and ocean engineering, 1990. **116**(3): p. 307-323.
114. Sumer, B.M. and J. Fredsøe, *Scour around pipelines in combined waves and current*. 1996, American Society of Mechanical Engineers, New York, NY (United States).
115. Sumer, B.M., H.R. Jensen, Y. Mao, and J. Fredsøe, *Effect of lee-wake on scour below pipelines in current.* Journal of Waterway, Port, Coastal, and Ocean Engineering, 1988. **114**(5): p. 599-614.
116. Sun, R. and H. Xiao, *SediFoam: A general-purpose, open-source CFD–DEM solver for particle-laden flow with emphasis on sediment transport.* Computers & Geosciences, 2016. **89**: p. 207-219.
117. Thomas, D.G., *Transport characteristics of suspension: VIII. A note on the viscosity of Newtonian suspensions of uniform spherical particles.* Journal of Colloid Science, 1965. **20**(3): p. 267-277.
118. Toorman, E., C. Lacor, E. Awad, M.W. Heredia, and P. Widera. *Scale problems in 3D sediment transport models and suggestions to overcome them*. Qualité des Eaux Marines. Vol. 1-8, 2007. Colloque SHF Pollution Maritime, Paris: Société Hydraulique de France.
119. Toorman, E.A., *Vertical mixing in the fully developed turbulent layer of sediment-laden open-channel flow.* Journal of hydraulic engineering, 2008. **134**(9): p. 1225-1235.
120. Toorman, E.A., *Errata and Addendum for "Vertical Mixing in the Fully Developed Turbulent Layer of Sediment-Laden Open-Channel Flow" by EA Toorman.* Journal of Hydraulic Engineering, 2009. **135**(6): p. 538-538.
121. Van Bang, D.P., E. Lefrancois, P. Sergent, and F. Bertrand, *MRI experimental and finite elements modeling of the sedimentation-consolidation of mud.* La Houille Blanche, 2008(3): p. 39-44.
122. Versteeg, H.K. and W. Malalasekera, *An introduction to computational fluid dynamics: the finite volume method*. 2007: Pearson Education.
123. Wallis, G.B., *One-dimensional two-phase flow.* 1969.
124. Weisstein, E.W., *Sphere packing.* 2003.
125. Weller, H.G., *A new approach to VOF-based interface capturing methods for incompressible and compressible flow.* OpenCFD Ltd., Report TR/HGW, 2008. **4**.
126. Weller, H.G., G. Tabor, H. Jasak, and C. Fureby, *A tensorial approach to computational continuum mechanics using object-oriented techniques.* Computers in physics, 1998. **12**(6): p. 620-631.

ACCEPTED MANUSCRIPT

127. Widera, P., *Study of sediment transport processes using Reynolds Averaged Navier-Stokes and Large Eddy Simulation*. 2011, PhD Thesis, Faculty of Engineering, Vrije Universiteit Brussel, S. 205.
128. Więckowski, Z., *The material point method in large strain engineering problems.* Computer methods in applied mechanics and engineering, 2004. **193**(39-41): p. 4417-4438.
129. Wong, W.H., *A comparison of wave-dominated cross-shore sand transport models*. 2010, University of Twente.
130. Zalesak, S.T., *Fully multidimensional flux-corrected transport algorithms for fluids.* Journal of computational physics, 1979. **31**(3): p. 335-362.
131. Zhang, K. and A. Acrivos, *Viscous resuspension in fully developed laminar pipe flows.* International journal of multiphase flow, 1994. **20**(3): p. 579-591.
132. Zhang, Q. and K. Kamrin, *Microscopic description of the granular fluidity field in nonlocal flow modeling.* Physical review letters, 2017. **118**(5): p. 058001.
133. Zhong, D., G. Wang, and B. Wu, *Drift velocity of suspended sediment in turbulent open channel flows.* Journal of Hydraulic Engineering, 2013. **140**(1): p. 35-47.

ACCEPTED MANUSCRIPT

ACCEPTED MANUSCRIPT

7. Appendix A: Mathematical derivation of model equations

A1. Basic mixture definitions and relations

Volume fractions:

α_s : Sediment volume fraction

α_w : Water volume fraction

α_a : Air volume fraction

γ : Sediment-water mixture (hereinafter the suspension) volume fraction. The following relations follows from those definitions:

$$\gamma \equiv \alpha_s + \alpha_w \quad \Rightarrow \quad \alpha_w = \gamma - \alpha_s \tag{A1.1}$$

$$\sum_k \alpha_k = \alpha_s + \alpha_w + \alpha_a = \gamma + \alpha_a = 1 \quad \Rightarrow \quad \alpha_a = 1 - \gamma \tag{A1.2}$$

Mixture densities:

ρ_m : Suspension density

ρ : Sediment-water-air mixture (hereinafter the mixture) density, given by:

$$\rho = \sum_k \alpha_k \bar{\bar{\rho}}_k = \alpha_s \rho_s + \alpha_w \rho_w + \alpha_a \rho_a = \gamma \rho_m + \alpha_a \rho_a \tag{A1.3}$$

Note that the water, sediment and air (phase averaged) densities in this analysis are considered constant. This is valid assumption for non-cohesive sediment transport in free surface flow at low Mach number where the whole mixture is modeled as an in-compressible fluid.

The suspension density ρ_m definition follows from equation (A1.3) as:

$$\rho_m = \frac{\alpha_s \rho_s + \alpha_w \rho_w}{\gamma} \tag{A1.4}$$

Mixture mass weighted velocities:

The velocity of mixture center of mass is given by:

$$\mathbf{v} = \frac{1}{\rho} \sum_k \alpha_k \bar{\bar{\rho}}_k \hat{\mathbf{v}}_k = \frac{\alpha_s \rho_s \mathbf{v}_s + \alpha_w \rho_w \mathbf{v}_w + \alpha_a \rho_a \mathbf{v}_a}{\rho} = \frac{\gamma \rho_m \mathbf{v}_m + \alpha_a \rho_a \mathbf{v}_a}{\rho} \tag{A1.5}$$

In equation (A1.5) all phasic velocities are mass weighted also. The suspension mass weighted velocity $\boldsymbol{v}_m$ is given by:

$$\mathbf{v}_m = \frac{\alpha_s \rho_s \mathbf{v}_s + \alpha_w \rho_w \mathbf{v}_w}{\gamma \rho_m} \tag{A1.6}$$

Mixture volumetric flux:

The mixture volumetric flux or the mixture center of volume velocity is defined as:

$$\boldsymbol{j} = \sum_k \alpha_k \hat{\mathbf{v}}_k = \alpha_s \mathbf{v}_s + \alpha_w \mathbf{v}_w + \alpha_a \mathbf{v}_a = \gamma \boldsymbol{j}_m + \alpha_a \mathbf{v}_a \tag{A1.7}$$

ACCEPTED MANUSCRIPT

The suspension volumetric flux (or velocity of center of volume) $\boldsymbol{j}_m$ is given by:

$$\boldsymbol{j}_m = \frac{\alpha_s \mathbf{v}_s + \alpha_w \mathbf{v}_w}{\gamma} \tag{A1.8}$$

Relative velocities:

The relative velocity between clear water and sediment ($\mathbf{w}$), and between the suspension and air ($\mathbf{U}_c$), are defined as:

$$\begin{aligned} \mathbf{w} &= \mathbf{v}_s - \mathbf{v}_w \\ \mathbf{U}_c &= \mathbf{v}_m - \mathbf{v}_a \end{aligned} \tag{A1.9}$$

A2. Advection term in the momentum equation of 3-phase flow

First we define the diffusion velocities of sediment, water and air as:

$$\begin{aligned} \mathbf{v}_{\mathrm{d},s} &= \mathbf{v}_s - \mathbf{v}_m \\ \mathbf{v}_{d,w} &= \mathbf{v}_w - \mathbf{v}_m \\ \mathbf{v}_{d,a} &= \mathbf{v}_a - \mathbf{v} \end{aligned} \tag{A2.1}$$

Each diffusion velocity can be re-written in term of relative velocity as follows:

$$\begin{aligned} \mathbf{v}_{\mathrm{d},s} &= \mathbf{v}_s - \mathbf{v}_m = \mathbf{v}_s - \frac{\alpha_s \rho_s \mathbf{v}_s + \alpha_w \rho_w \mathbf{v}_w}{\gamma \rho_m} = \mathbf{v}_s - \frac{\alpha_s \rho_s \mathbf{v}_s + \alpha_w \rho_w (\mathbf{v}_s - \mathbf{w})}{\gamma \rho_m} \\ &= \mathbf{v}_s - \frac{(\alpha_s \rho_s + \alpha_w \rho_w)\mathbf{v}_s - \alpha_w \rho_w \mathbf{w}}{\gamma \rho_m} = \mathbf{v}_s - \frac{\gamma \rho_m \mathbf{v}_s - \alpha_w \rho_w \mathbf{w}}{\gamma \rho_m} = \frac{\alpha_w \rho_w}{\gamma \rho_m}\mathbf{w} \end{aligned} \tag{A2.2}$$

$$\begin{aligned} \mathbf{v}_{d,w} &= \mathbf{v}_w - \mathbf{v}_m = \mathbf{v}_w - \frac{\alpha_s \rho_s \mathbf{v}_s + \alpha_w \rho_w \mathbf{v}_w}{\gamma \rho_m} = \mathbf{v}_w - \frac{\alpha_s \rho_s (\mathbf{v}_w + \mathbf{w}) + \alpha_w \rho_w \mathbf{v}_w}{\gamma \rho_m} \\ &= \mathbf{v}_w - \frac{(\alpha_s \rho_s + \alpha_w \rho_w)\mathbf{v}_w + \alpha_s \rho_s \mathbf{w}}{\gamma \rho_m} = \mathbf{v}_w - \frac{\gamma \rho_m \mathbf{v}_w + \alpha_s \rho_s \mathbf{w}}{\gamma \rho_m} = -\frac{\alpha_s \rho_s}{\gamma \rho_m}\mathbf{w} \end{aligned} \tag{A2.3}$$

$$\begin{aligned} \mathbf{v}_{d,a} &= \mathbf{v}_a - \mathbf{v} = \mathbf{v}_a - \frac{\gamma \rho_m \mathbf{v}_m + \alpha_a \rho_a \mathbf{v}_a}{\rho} = \mathbf{v}_a - \frac{\gamma \rho_m (\mathbf{U}_c + \mathbf{v}_a) + \alpha_a \rho_a \mathbf{v}_a}{\rho} \\ &= \boldsymbol{v}_a - \frac{\gamma \rho_m \mathbf{U}_c + (\gamma \rho_m + \alpha_a \rho_a)\mathbf{v}_a}{\rho} = \boldsymbol{v}_a - \frac{\gamma \rho_m \mathbf{U}_c + \rho \mathbf{v}_a}{\rho} = -\frac{\gamma \rho_m}{\rho}\mathbf{U}_c \end{aligned} \tag{A2.4}$$

Substituting (A2.1) into the advection term:

$$\begin{aligned} \sum_k \alpha_k \rho_k \mathbf{v}_k \mathbf{v}_k &= \alpha_s \rho_s \mathbf{v}_s (\mathbf{v}_m + \mathbf{v}_{\mathrm{d},s}) + \alpha_w \rho_w \mathbf{v}_w (\mathbf{v}_m + \mathbf{v}_{d,w}) + \alpha_a \rho_a \mathbf{v}_a (\mathbf{v} + \mathbf{v}_{d,a}) \\ &= (\alpha_s \rho_s \mathbf{v}_s + \alpha_w \rho_w \mathbf{v}_w)\mathbf{v}_m + \alpha_a \rho_a \mathbf{v}_a \mathbf{v} + \alpha_s \rho_s \mathbf{v}_s \mathbf{v}_{\mathrm{d},s} + \alpha_w \rho_w \mathbf{v}_w \mathbf{v}_{d,w} + \alpha_a \rho_a \mathbf{v}_a \mathbf{v}_{d,a} \\ &= \gamma \rho_m \mathbf{v}_m \mathbf{v}_m + \alpha_a \rho_a \mathbf{v}_a \mathbf{v} + \alpha_s \rho_s \mathbf{v}_s \mathbf{v}_{\mathrm{d},s} + \alpha_w \rho_w \mathbf{v}_w \mathbf{v}_{d,w} + \alpha_a \rho_a \mathbf{v}_a \mathbf{v}_{d,a} \end{aligned} \tag{A2.5}$$

The 1st and 2nd terms in the RHS of (A2.5) can be written as:

$$\begin{aligned}\gamma\rho_m\mathbf{v}_m\mathbf{v}_m+\alpha_a\rho_a\mathbf{v}_a\mathbf{v}&=\gamma\rho_m\mathbf{v}_m\left(\mathbf{v}_m-\mathbf{v}\right)+\left(\gamma\rho_m\mathbf{v}_m+\alpha_a\rho_a\mathbf{v}_a\right)\mathbf{v}\\&=\rho\mathbf{v}\mathbf{v}+\gamma\rho_m\mathbf{v}_m\left(\mathbf{v}_m-\mathbf{v}\right)\end{aligned}\tag{A2.6}$$

The 3rd and 4th term in the RHS of (A2.5) can be written with help of (A2.2) and (A2.3) as:

$$\begin{aligned}\alpha_s\rho_s\mathbf{v}_s\mathbf{v}_{\mathrm{d},s}+\alpha_w\rho_w\mathbf{v}_w\mathbf{v}_{d,w}&=\alpha_s\rho_s\left(\mathbf{v}_w+\mathbf{w}\right)\left(\frac{\alpha_w\rho_w}{\gamma\rho_m}\mathbf{w}\right)+\alpha_w\rho_w\mathbf{v}_w\left(-\frac{\alpha_s\rho_s}{\gamma\rho_m}\mathbf{w}\right)\\&=\alpha_s\rho_s\frac{\alpha_w\rho_w}{\gamma\rho_m}\mathbf{v}_w\mathbf{w}-\alpha_w\rho_w\frac{\alpha_s\rho_s}{\gamma\rho_m}\mathbf{v}_w\mathbf{w}+\alpha_s\rho_s\frac{\alpha_w\rho_w}{\gamma\rho_m}\mathbf{w}\mathbf{w}\\&=\alpha_s\left(1-\frac{\alpha_s}{\gamma}\right)\frac{\rho_s\rho_w}{\rho_m}\mathbf{w}\mathbf{w}\end{aligned}\tag{A2.7}$$

The last term in the RHS of (A2.5) can be written with help of (A2.4) as:

$$\begin{aligned}\alpha_a\rho_a\mathbf{v}_a\mathbf{v}_{d,a}&=-\alpha_a\rho_a\left(\mathbf{v}_m-\mathbf{U}_c\right)\left(\frac{\gamma\rho_m}{\rho}\mathbf{U}_c\right)\\&=\gamma\left(1-\gamma\right)\frac{\rho_a\rho_m}{\rho}\mathbf{U}_c\mathbf{U}_c-\gamma\left(1-\gamma\right)\frac{\rho_a\rho_m}{\rho}\mathbf{v}_m\mathbf{U}_c\end{aligned}\tag{A2.8}$$

So, using equations (A2.6) to (A2.8), the advection term can be rewritten in term of mixture and relative velocities as follows:

$$\begin{aligned}\sum_k\alpha_k\rho_k\mathbf{v}_k\mathbf{v}_k&=\rho\mathbf{v}\mathbf{v}+\alpha_s\left(1-\frac{\alpha_s}{\gamma}\right)\frac{\rho_s\rho_w}{\rho_m}\mathbf{w}\mathbf{w}+\gamma\left(1-\gamma\right)\frac{\rho_a\rho_m}{\rho}\mathbf{U}_c\mathbf{U}_c\\&\quad+\gamma\rho_m\mathbf{v}_m\left(\mathbf{v}_m-\mathbf{v}\right)-\gamma\left(1-\gamma\right)\frac{\rho_a\rho_m}{\rho}\mathbf{v}_m\mathbf{U}_c\end{aligned}\tag{A2.9}$$

Moreover, one can prove that the last two terms cancels each other, as follow:

$$\begin{aligned}\gamma\rho_m\mathbf{v}_m\left(\mathbf{v}_m-\mathbf{v}\right)-\gamma\left(1-\gamma\right)\frac{\rho_a\rho_m}{\rho}\mathbf{v}_m\mathbf{U}_c&=\gamma\rho_m\mathbf{v}_m\left(\mathbf{v}_m-\mathbf{v}\right)-\gamma\rho_m\mathbf{v}_m\frac{\alpha_a\rho_a}{\rho}\left(\mathbf{v}_m-\mathbf{v}_a\right)\\&=\gamma\rho_m\mathbf{v}_m\left(\mathbf{v}_m-\mathbf{v}-\frac{\alpha_a\rho_a}{\rho}\left(\mathbf{v}_m-\mathbf{v}_a\right)\right)=\gamma\rho_m\mathbf{v}_m\left(\mathbf{v}_m\left(1-\frac{\alpha_a\rho_a}{\rho}\right)+\frac{\alpha_a\rho_a}{\rho}\mathbf{v}_a-\mathbf{v}\right)\\&=\gamma\rho_m\mathbf{v}_m\left(\frac{\gamma\rho_m}{\rho}\mathbf{v}_m+\frac{\alpha_a\rho_a}{\rho}\mathbf{v}_a-\mathbf{v}\right)=\gamma\rho_m\mathbf{v}_m\left(\frac{1}{\rho}\left(\gamma\rho_m\mathbf{v}_m+\alpha_a\rho_a\mathbf{v}_a\right)-\mathbf{v}\right)\\&=\gamma\rho_m\mathbf{v}_m\left(\frac{1}{\rho}\left(\rho\mathbf{v}\right)-\mathbf{v}\right)=0\end{aligned}\tag{A2.10}$$

So, the final form of the advection term is given as:

$$\sum_k\alpha_k\rho_k\mathbf{v}_k\mathbf{v}_k=\rho\mathbf{v}\mathbf{v}+\alpha_s\left(1-\frac{\alpha_s}{\gamma}\right)\frac{\rho_s\rho_w}{\rho_m}\mathbf{w}\mathbf{w}+\gamma\left(1-\gamma\right)\frac{\rho_a\rho_m}{\rho}\mathbf{U}_c\mathbf{U}_c\tag{A2.11}$$

A3. Kinematic relations between suspension and mixture

ACCEPTED MANUSCRIPT

Kinematic equation for $\boldsymbol{j}_m$

$$\begin{aligned}\boldsymbol{j} &\equiv \gamma \boldsymbol{j}_m + (1-\gamma)\mathbf{v}_a \\ \boldsymbol{j}_m - \boldsymbol{j} &= \boldsymbol{j}_m - \gamma \boldsymbol{j}_m - (1-\gamma)\mathbf{v}_a = (1-\gamma)\boldsymbol{j}_m - (1-\gamma)\boldsymbol{v}_a \\ &= (1-\gamma)(\boldsymbol{j}_m - \boldsymbol{v}_a) = (1-\gamma)\boldsymbol{j}_{m\text{-}a} \\ \boldsymbol{j}_m &= \boldsymbol{j} + (1-\gamma)\boldsymbol{j}_{m\text{-}a}\end{aligned} \tag{A3.1}$$

Where $\boldsymbol{j}_{m\text{-}a}$ is the relative volumetric flux between the suspension and air. This term can be written as function of the relative velocities as follows:

$$\begin{aligned}\boldsymbol{j}_{m\text{-}a} &\equiv \boldsymbol{j}_m - \mathbf{v}_a = \frac{\alpha_s \mathbf{v}_s + \alpha_w \mathbf{v}_w}{\gamma} - \mathbf{v}_a + \mathbf{v}_m - \mathbf{v}_m = \mathbf{U}_c + \frac{\alpha_s \mathbf{v}_s + \alpha_w \mathbf{v}_w}{\gamma} - \mathbf{v}_m \\ &= \mathbf{U}_c + \frac{\alpha_s \mathbf{v}_s + \alpha_w \mathbf{v}_w}{\gamma} - \frac{\alpha_s \rho_s \mathbf{v}_s + \alpha_w \rho_w \mathbf{v}_w}{\gamma \rho_m} \\ &= \mathbf{U}_c + \frac{\alpha_s \mathbf{v}_s}{\gamma}\left(1 - \frac{\rho_s}{\rho_m}\right) + \frac{\alpha_w \mathbf{v}_w}{\gamma}\left(1 - \frac{\rho_w}{\rho_m}\right)\end{aligned} \tag{A3.2}$$

The brackets in the last two terms of (A3.2) can be written as:

$$\begin{aligned}1 - \frac{\rho_s}{\rho_m} &= 1 - \frac{\gamma \rho_s}{\alpha_s \rho_s + \alpha_w \rho_w} = 1 - \frac{\gamma S}{\alpha_s S + \alpha_w} = \frac{\alpha_s S + \alpha_w - \gamma S}{\alpha_s S + \gamma - \alpha_s} \\ &= \frac{(\gamma - \alpha_s) - S(\gamma - \alpha_s)}{\gamma - \alpha_s(1-S)} = \frac{(\gamma - \alpha_s)(1-S)}{\gamma - \alpha_s(1-S)}\end{aligned} \tag{A3.3}$$

$$\begin{aligned}1 - \frac{\rho_w}{\rho_m} &= 1 - \frac{\gamma \rho_w}{\alpha_s \rho_s + \alpha_w \rho_w} = 1 - \frac{\gamma}{\alpha_s S + \alpha_w} = \frac{\alpha_s S + \alpha_w - \gamma}{\alpha_s S + \gamma - \alpha_s} \\ &= \frac{\alpha_s S - \alpha_s}{\gamma - \alpha_s(1-S)} = \frac{-\alpha_s(1-S)}{\gamma - \alpha_s(1-S)}\end{aligned} \tag{A3.4}$$

Where S is the specific gravity of sand. Substituting (A3.3) & (A3.4) into (A3.2) we get:

$$\begin{aligned}\boldsymbol{j}_{m\text{-}a} &= \mathbf{U}_c + \frac{\alpha_s \mathbf{v}_s}{\gamma}\frac{(\gamma - \alpha_s)(1-S)}{\gamma - \alpha_s(1-S)} - \frac{(\gamma - \alpha_s)\mathbf{v}_w}{\gamma}\frac{\alpha_s(1-S)}{\gamma - \alpha_s(1-S)} \\ &= \mathbf{U}_c + \frac{\alpha_s(\gamma - \alpha_s)(1-S)}{\gamma(\gamma - \alpha_s(1-S))}(\mathbf{v}_s - \mathbf{v}_w) \\ &= \mathbf{U}_c + \frac{\alpha_s \alpha_w (1-S)}{\gamma(\gamma - \alpha_s(1-S))}\mathbf{w}\end{aligned} \tag{A3.5}$$

ACCEPTED MANUSCRIPT

Kinematic equation for j

$$\begin{aligned}
\boldsymbol{j} &\equiv \sum_k \alpha_k \hat{\mathbf{v}}_k = \alpha_s \mathbf{v}_s + \alpha_w \mathbf{v}_w + \alpha_a \mathbf{v}_a = \gamma \boldsymbol{j}_m + \alpha_a \mathbf{v}_a \\
\boldsymbol{j} &= \frac{\rho}{\rho}\left(\alpha_s \mathbf{v}_s + \alpha_w \mathbf{v}_w + \alpha_a \mathbf{v}_a\right) = \frac{\alpha_s \rho_s + \alpha_w \rho_w + \alpha_a \rho_a}{\rho}\left(\alpha_s \mathbf{v}_s + \alpha_w \mathbf{v}_w + \alpha_a \mathbf{v}_a\right) \\
&= \frac{1}{\rho}\left(\alpha_s \alpha_s \rho_s \mathbf{v}_s + \alpha_s \rho_s \alpha_w \mathbf{v}_w + \alpha_s \rho_s \alpha_a \mathbf{v}_a + \alpha_w \rho_w \alpha_s \mathbf{v}_s + \alpha_w \alpha_w \rho_w \mathbf{v}_w \right. \\
&\left. + \alpha_w \rho_w \alpha_a \mathbf{v}_a + \alpha_a \rho_a \alpha_s \mathbf{v}_s + \alpha_a \rho_a \alpha_w \mathbf{v}_w + \alpha_a \alpha_a \rho_a \mathbf{v}_a\right)
\end{aligned} \tag{A3.6}$$

In(A3.6), the terms with compatible subscripts can be further manipulated as follows

$$\begin{aligned}
\alpha_s \alpha_s \rho_s \mathbf{v}_s &= \alpha_s\left(\rho_s \mathbf{v}_s - \left(1-\alpha_s\right)\rho_s \mathbf{v}_s\right) = \alpha_s\left(\rho_s \mathbf{v}_s - \left(\alpha_w + \alpha_a\right)\rho_s \mathbf{v}_s\right) \\
&= \alpha_s \rho_s \mathbf{v}_s - \alpha_s \alpha_w \rho_s \mathbf{v}_s - \alpha_s \alpha_a \rho_s \mathbf{v}_s \\
\alpha_w \alpha_w \rho_w \mathbf{v}_w &= \alpha_w\left(\rho_w \mathbf{v}_w - \left(1-\alpha_w\right)\rho_w \mathbf{v}_w\right) = \alpha_w\left(\rho_w \mathbf{v}_w - \left(\alpha_s + \alpha_a\right)\rho_w \mathbf{v}_w\right) \\
&= \alpha_w \rho_w \mathbf{v}_w - \alpha_w \alpha_s \rho_w \mathbf{v}_w - \alpha_w \alpha_a \rho_w \mathbf{v}_w \\
\alpha_a \alpha_a \rho_a \mathbf{v}_a &= \alpha_a\left(\rho_a \mathbf{v}_a - \left(1-\alpha_a\right)\rho_a \mathbf{v}_a\right) = \alpha_a \rho_a \mathbf{v}_a - \alpha_a\left(\alpha_s + \alpha_w\right)\rho_a \mathbf{v}_a \\
&= \alpha_a \rho_a \mathbf{v}_a - \alpha_a \alpha_s \rho_a \mathbf{v}_a - \alpha_a \alpha_w \rho_a \mathbf{v}_a
\end{aligned} \tag{A3.7}$$

Substituting (A3.7) in (A3.6) we get:

$$\begin{aligned}
\boldsymbol{j} &= \frac{1}{\rho}\left(\alpha_s \rho_s \mathbf{v}_s + \alpha_w \rho_w \mathbf{v}_w + \alpha_a \rho_a \mathbf{v}_a - \alpha_s \alpha_w \rho_s \mathbf{v}_s - \alpha_s \alpha_a \rho_s \mathbf{v}_s + \alpha_s \alpha_w \rho_s \mathbf{v}_w \right. \\
&\quad + \alpha_s \alpha_a \rho_s \mathbf{v}_a + \alpha_w \alpha_s \rho_w \mathbf{v}_s - \alpha_w \alpha_s \rho_w \mathbf{v}_w - \alpha_w \alpha_a \rho_w \mathbf{v}_w + \alpha_w \alpha_a \rho_w \mathbf{v}_a \\
&\left. \quad + \alpha_a \alpha_s \rho_a \mathbf{v}_s + \alpha_a \alpha_w \rho_a \mathbf{v}_w - \alpha_a \alpha_s \rho_a \mathbf{v}_a - \alpha_a \alpha_w \rho_a \mathbf{v}_a\right) \\
&= \mathbf{v} + \frac{1}{\rho}\left(-\left(\rho_s - \rho_w\right)\alpha_w \alpha_s \mathbf{v}_s + \left(\rho_s - \rho_w\right)\alpha_s \alpha_w \mathbf{v}_w - \alpha_a\left(\alpha_s \rho_s \mathbf{v}_s + \alpha_w \rho_w \mathbf{v}_w\right)\right. \\
&\left. \quad + \left(\alpha_s \rho_s + \alpha_w \rho_w\right)\alpha_a \mathbf{v}_a + \alpha_a \rho_a\left(\alpha_s \mathbf{v}_s + \alpha_w \mathbf{v}_w\right) - \left(\alpha_s + \alpha_w\right)\alpha_a \rho_a \mathbf{v}_a\right) \\
&= \mathbf{v} - \alpha_w \alpha_s \frac{\left(\rho_s - \rho_w\right)}{\rho}\mathbf{w} + \frac{1}{\rho}\left(-\alpha_a \gamma \rho_m \mathbf{v}_m + \gamma \alpha_a \rho_m \mathbf{v}_a + \alpha_a \rho_a \gamma\left(\boldsymbol{j}_m - \mathbf{v}_a\right)\right) \\
&= \mathbf{v} - \alpha_w \alpha_s \frac{\left(\rho_s - \rho_w\right)}{\rho}\mathbf{w} + \frac{1}{\rho}\left(-\alpha_a \gamma \rho_m\left(\mathbf{v}_m - \mathbf{v}_a\right) + \alpha_a \rho_a \gamma \boldsymbol{j}_{m\text{-}a}\right) \\
&= \mathbf{v} - \alpha_s\left(\gamma - \alpha_s\right)\frac{\left(\rho_s - \rho_w\right)}{\rho}\mathbf{w} - \gamma\left(1-\gamma\right)\frac{\rho_m}{\rho}\mathbf{U}_c + \gamma\left(1-\gamma\right)\frac{\rho_a}{\rho}\boldsymbol{j}_{m\text{-}a}
\end{aligned} \tag{A3.8}$$

Note that $\boldsymbol{j}_{m\text{-}a}$ in the last term in RHS of (A3.8) is given by equation (A3.5) which shows that this term is also function of the relative velocities. So, equation (A3.8) gives the mixture center of volume velocity as a function of the mixture center of mass velocity and relative velocities. It also clearly shows that if the relative velocities between different phases vanished, both center of mass and center of volume velocity of the mixture will be equal.

Using the definition of $\boldsymbol{j}_{m\text{-}a}$ in equation(A3.5), we get:

ACCEPTED MANUSCRIPT

$$\boldsymbol{j} \approx \mathbf{v} - \alpha_s\left(\gamma - \alpha_s\right)\frac{\rho_s - \rho_w}{\rho}\mathbf{w} - \gamma\left(1-\gamma\right)\frac{\rho_m - \rho_a}{\rho}\mathbf{U}_c \tag{A3.9}$$

Note that this equation gives **j** with very small error (in order of 0.1%).

A4. Kinematic equations for sediment and water velocities

Kinematic equation for the sediment velocity $\mathbf{v}_s$

$$\begin{aligned}\boldsymbol{j}_m &\equiv \frac{\alpha_s\mathbf{v}_s + \alpha_w\mathbf{v}_w}{\gamma} = \frac{\alpha_s\mathbf{v}_s + \alpha_w\left(\mathbf{v}_s - \mathbf{w}\right)}{\gamma} = \frac{\left(\alpha_s + \alpha_w\right)\mathbf{v}_s - \alpha_w\mathbf{w}}{\gamma} = \mathbf{v}_s - \frac{\alpha_w}{\gamma}\mathbf{w} \\ \mathbf{v}_s &= \boldsymbol{j}_m + \frac{\alpha_w}{\gamma}\mathbf{w}\end{aligned} \tag{A4.1}$$

We recall form (A3.1) that:

$$\boldsymbol{j}_m = \boldsymbol{j} + \left(1-\gamma\right)\boldsymbol{j}_{m\text{-}a}$$

Then we substitute for **j** and $\boldsymbol{j}_{m\text{-}a}$ from (A3.9) and (A3.5), respectively, we get:

$$\begin{aligned}\boldsymbol{j}_m &= \mathbf{v} - \alpha_s\left(\gamma - \alpha_s\right)\frac{\rho_s - \rho_w}{\rho}\mathbf{w} - \gamma\left(1-\gamma\right)\frac{\rho_m - \rho_a}{\rho}\mathbf{U}_c \\ &\quad + \left(1-\gamma\right)\mathbf{U}_c + \left(1-\gamma\right)\frac{\alpha_s\alpha_w\left(1-S\right)}{\gamma\left(\gamma - \alpha_s\left(1-S\right)\right)}\mathbf{w} \\ &= \mathbf{v} + \left(-\alpha_w\alpha_s\frac{\rho_s - \rho_w}{\rho} + \frac{\alpha_s\alpha_w\alpha_a\left(1-S\right)}{\gamma\left(\gamma - \alpha_s\left(1-S\right)\right)}\right)\mathbf{w} + \left(1 - \gamma\frac{\rho_m - \rho_a}{\rho}\right)\alpha_a\mathbf{U}_c\end{aligned} \tag{A4.2}$$

Substitute from (A4.2) into (A4.1), we get:

$$\mathbf{v}_s = \mathbf{v} + \left(\frac{\alpha_w}{\gamma} - \alpha_w\alpha_s\frac{\rho_s - \rho_w}{\rho} + \frac{\alpha_a\alpha_s\alpha_w\left(1-S\right)}{\gamma\left(\alpha_w + \alpha_s S\right)}\right)\mathbf{w} + \left(1 - \gamma\frac{\rho_m - \rho_a}{\rho}\right)\alpha_a\mathbf{U}_c \tag{A4.3}$$

Kinematic equation for the water velocity $\mathbf{v}_w$

$$\begin{aligned}\boldsymbol{j}_m &\equiv \frac{\alpha_s\mathbf{v}_s + \alpha_w\mathbf{v}_w}{\gamma} = \frac{\alpha_s\left(\mathbf{v}_w + \mathbf{w}\right) + \alpha_w\mathbf{v}_w}{\gamma} = \frac{\left(\alpha_s + \alpha_w\right)\mathbf{v}_w + \alpha_s\mathbf{w}}{\gamma} = \mathbf{v}_w + \frac{\alpha_s}{\gamma}\mathbf{w} \\ \mathbf{v}_w &= \boldsymbol{j}_m - \frac{\alpha_s}{\gamma}\mathbf{w}\end{aligned} \tag{A4.4}$$

Substitute from (A4.2) into (A4.4), we get:

$$\mathbf{v}_w = \mathbf{v} + \left(-\frac{\alpha_s}{\gamma} - \alpha_w\alpha_s\frac{\rho_s - \rho_w}{\rho} + \frac{\alpha_s\alpha_w\alpha_a\left(1-S\right)}{\gamma\left(\gamma - \alpha_s\left(1-S\right)\right)}\right)\mathbf{w} + \left(1 - \gamma\frac{\rho_m - \rho_a}{\rho}\right)\alpha_a\mathbf{U}_c \tag{A4.5}$$

ACCEPTED MANUSCRIPT